Front. Mech. Eng. 2020, 15(4): 517–537
https://doi.org/10.1007/s11465-020-0589-z

RESEARCH ARTICLE

Yin ZHANG, Jianwei WU, Kunpeng XING, Zhongpu WEN, Jiubin TAN

Evaluation of measurement uncertainty of the high-speed variable-slit system based on the Monte Carlo method

Abstract This paper presents a dynamic and static error transfer model and uncertainty evaluation method for a high-speed variable-slit system based on a two-dimensional orthogonal double-layer air-floating guide rail structure. The motion accuracy of the scanning blade is affected by both the moving component it is attached to and the moving component of the following blade during high-speed motion. First, an error transfer model of the high-speed variable-slit system is established, and the influence coefficients are calculated for each source of error associated with the accuracy of the blade motion. Then, the maximum range of each error source is determined by simulation and experiment. Finally, the uncertainty of the blade displacement measurement is evaluated using the Monte Carlo method. The proposed model can evaluate the performance of the complex mechanical system and be used to guide the design.

Keywords air-floating guide rail, error transfer model, driving and following structure, dynamic error, uncertainty evaluation, Monte Carlo method

1 Introduction

Rapid advances in the semiconductor industry have led to the need for high-throughput photolithography systems that can produce semiconductor devices with enhanced performance at higher speeds. Therefore, the exposure system used in photolithography processes must provide high productivity, a low critical dimension, and a high overlay [1–4]. The optical illumination system of the lithography exposure machine is shown in Fig. 1. The high-speed variable slit system (HSVSS) is an important part of the optical illumination system. As shown in Fig. 1, the generated laser light propagated along the beam line and red arrows indicate the direction of laser propagation. The variable attenuator can adjust laser power and the integrator rod can homogenize laser exposure. On the path of laser propagation, energy sensor can detect laser power for precise power control and the HSVSS controls the position and size of the exposed area by driving a set of blades. Finally, the laser is exposure on the spot sensor through a series of optical lens. During the exposure process, the scanning blades are synchronized with the mask to prevent the beam from illuminating areas outside of the specified exposure field. Therefore, rapid acceleration and high precision of the blade movements are required. The performance of the HSVSS directly affects the performance of the lithography exposure machine and the quality of the resulting semiconductor chip.

Mechanical systems in lithography exposure machine usually require demanding functional requirements and performance index in a limited design space. Its functional requirements and performance indexes depend on the design of complex mechanical system. Based on the requirements of the optical illumination system, the four blades of the HSVSS must move along the same plane with high acceleration and at high speed. This requires each blade in the HSVSS to have two degrees of freedom. To meet these design requirements, a "driving and following" structure based on a two-dimensional orthogonal double-layer air-floating guide rail must be used as the motion transmission mechanism of the HSVSS. The key issue in the design of the HSVSS is the ability to drive the blades with high dynamic accuracy within such a complex structure. Establishing a dynamic and static error propagation model of the HSVSS and analyzing the influence of each error source on the blade displacement error can provide guidance for error compensation and determine

Received November 19, 2019; accepted February 20, 2020

Yin ZHANG, Jianwei WU (✉), Kunpeng XING, Zhongpu WEN, Jiubin TAN
Centre of Ultra-precision Optoelectronic Instrumentation Engineering, Harbin Institute of Technology, Harbin 150001, China; Key Laboratory of Ultra-precision Intelligent Instrumentation (Harbin Institute of Technology), Ministry of Industry and Information Technology, Harbin 150080, China
E-mail: wujianwei@hit.edu.cn

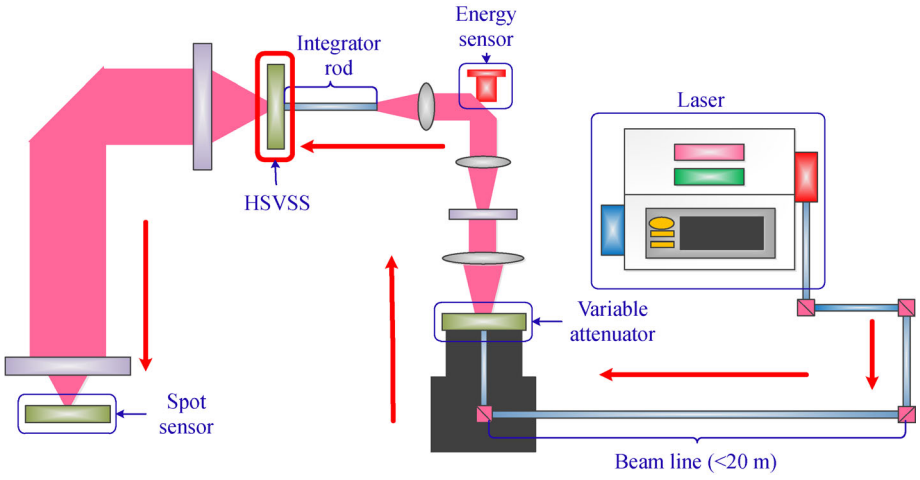

Fig. 1 Schematic diagram of the optical illumination system. HSVSS: High-speed variable slit system.

how error should be distributed in the design of the system [5–7]. However, error values cannot be obtained through experiments and simulations. Therefore, estimating the uncertainty of the blade displacement measurement is necessary to evaluate the system's performance [8–11]. Proposing different error modeling methods for different mechanical systems has become a hot research topic in the field of precision machinery.

Error modeling of precision mechanical systems has been extensively researched in the past. The homogeneous transformation matrix [12,13] and Denavit–Hartenberg transformation matrix [14] are widely used. Tang et al. [15] introduced a systematic approach to calculate the straightness and angular kinematic errors based on measurements of the guideway surface and fitting curve. Chen et al. [16] proposed a comprehensive error analysis method to uncover how geometric error propagates through every motion axis, and to identify the error parameters with the greatest impact on the tool posture error at the end of the kinematic chain. Tian et al. [17] presented a general systematic approach based on linear mapping for modelling the geometric error of machine tools due to manufacturing and assembly errors. Zhao et al. [18], Li et al. [19], Chen et al. [20], and Liu et al. [21] established error transformation models of five-axis machine tools, and proposed various methods of analyzing the error source sensitivity and identifying errors. Andolfatto et al. [22] and Liu et al. [23] evaluated the mechanical performance of a five-axis machine tool and an H-drive stage with an air bearing, respectively, and used the Monte Carlo method (MCM) in their analyses to assess measurement accuracy.

The error propagation models of structures in the above methods are either single-chain models or simple double-chain models [20]. Every blade in the HSVSS has two sets of structures (driving and following), each with two degrees of freedom. The error transmission of the driving structure and the following structure interact with each other. Furthermore, every blade should have high accuracy during high acceleration and at high speed. Therefore, it is necessary to develop a specific method for modelling the error and uncertainty of these unique structures.

An error analysis method for the HSVSS during high acceleration and high speed is proposed in this paper. First, an error transfer model of the HSVSS is established based on the theory of multi-body systems and the influence coefficient is calculated for each source of error. Then, the maximum error range of is obtained for each error value either using a finite element simulation or experimentally. Finally, the displacement measurement uncertainty results of the blades are evaluated using the MCM.

2 Driving and following structures of the HSVSS

As shown in Fig. 2, the HSVSS of the step-and-scan lithography exposure machine adjusts the exposure area by controlling the movements of four blades. Blades of the HSVSS form rectangular windows of different sizes at different positions. The red dots in Fig. 2 represent the center of the optical system, and the four blades are labelled as Y1, X1, Y2, and X2. During the exposure process, Blades X1 and X2 move in a stepwise motion along X direction, and Blades Y1 and Y2 scan along Y direction. To prevent light leakage from affecting the exposure quality, the four blades must remain on the same plane and have high motion accuracy during high acceleration and at high speed.

When the four blades are in the same plane, they cannot overlap, and every blade must move in two degrees of freedom at high speed and with high precision. The motion guiding mechanism of the blade is a two-dimensional orthogonal double-layer air-floating guide rail, as shown in Fig. 3. In this structure, the rail fixed to the basic mounting plate is referred to as the driving air-floating guide rail and the rail connected to the blade is called the air-floating

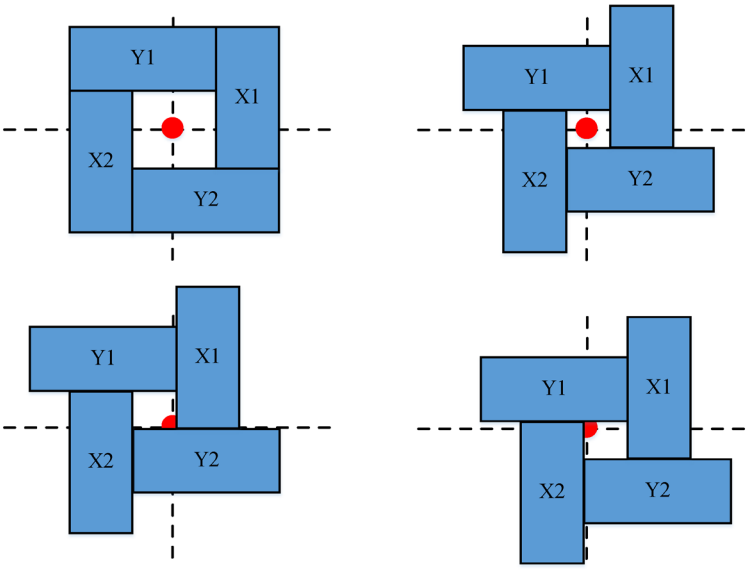

Fig. 2 Schematic drawing of the rectangular window.

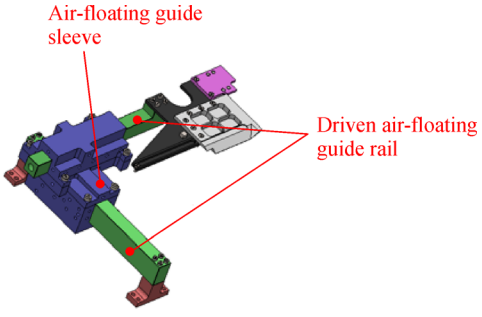

Fig. 3 Schematic diagram of two-dimensional orthogonal double-layer air-floating guide rail.

guide driven rail. Two perpendicular rails (driving rail and driven rail) are attached to the air-floating guide sleeve. The two air-floating guide rails and the air-floating guide sleeve can move relative to one another at high speed.

As shown in Fig. 4, the entire system consists of four blades and their guiding mechanism. The blade is installed on the blade holder and the blade holder is fixed on the driven rail. Adjacent blade holders are connected by linkage mechanism consisting of a magnet, two bearings, and a limiting device. Taking Blade Y1 as an example, when the blade moves along *Y* direction on the driving rail, it carries Blade X2 on the driven rail along the *Y* direction, as shown in Fig. 5. During this movement, Blade Y1 is the driving blade and Blade X2 is the following blade.

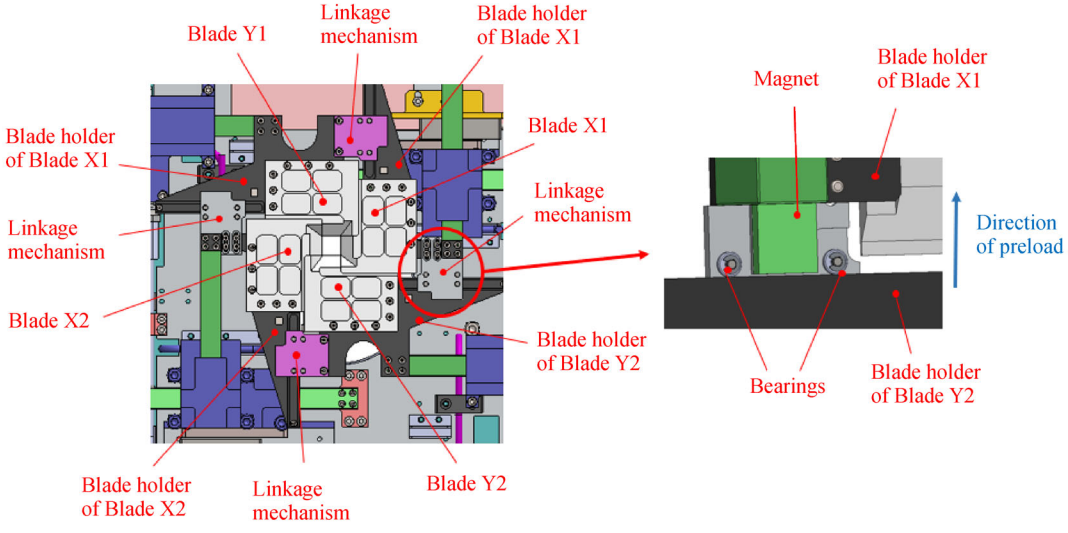

Fig. 4 Schematic diagram of blades and linkage mechanism.

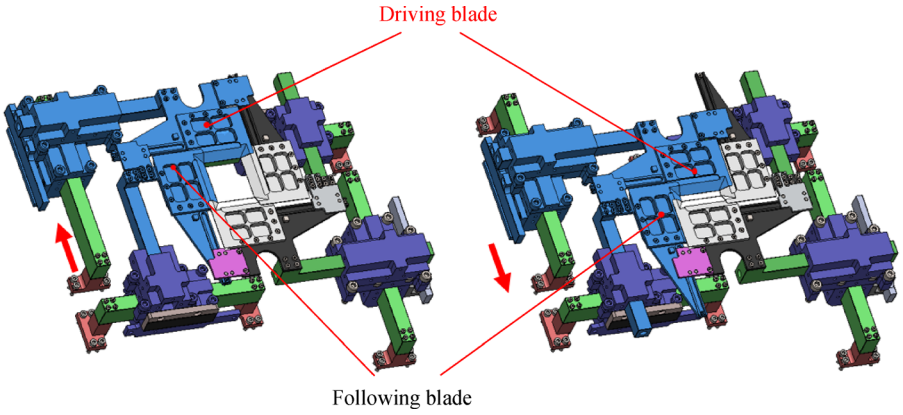

Fig. 5 Schematic illustration of motion of the driving blade and following blade (Blade Y1).

Bearings on the blade holder of Blades X2 and Y1 roll along the holder of Blades X1 and Y2, respectively, and the magnets add a preload between the bearings and blade holders. Thus, the motion error of the blade is mainly caused by the error of the moving component that it is attached to as well as the moving component of the next blade. Kinematic relationships of the blades are presented in Table 1.

Table 1 Kinematic relationships of blades

Driving blade	Following blade	Motionless blade
Y1	X2	X1, Y2
Y2	X1	X2, Y1
X1	Y1	X2, Y2
X2	Y2	X1, Y1

The overall structure of the HSVSS is shown in Fig. 6. The system is comprised of linear motors, air-floating guide rails, and moving components. The measurement feedback module is a linear scale grating ruler. The driving guide rail of the double-layer two-dimensional orthogonal air-floating guide rail is fixed on a basic mounting plate and the sleeve is directly driven by the linear motor. To achieve high control accuracy, a gravity compensation device is applied to the guide rail moving along Y direction and fixed behind the basic mounting plate.

3 Integrated error propagation model of the HSVSS

3.1 Error propagation model

The HSVSS is a mechanical system composed of several rigid bodies. The topology of the system can be described using a low-order array. Based on the previous section, it can be concluded that the motion error of the blade is caused by the error of the moving component the blade is attached to and the moving component of the following blade. As shown in Fig. 7(a), the single blade displacement

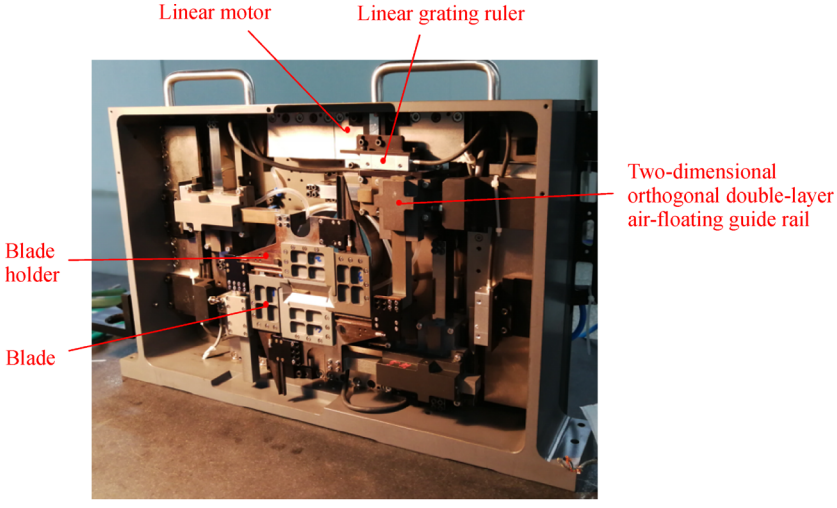

Fig. 6 Photograph of the overall HSVSS structure.

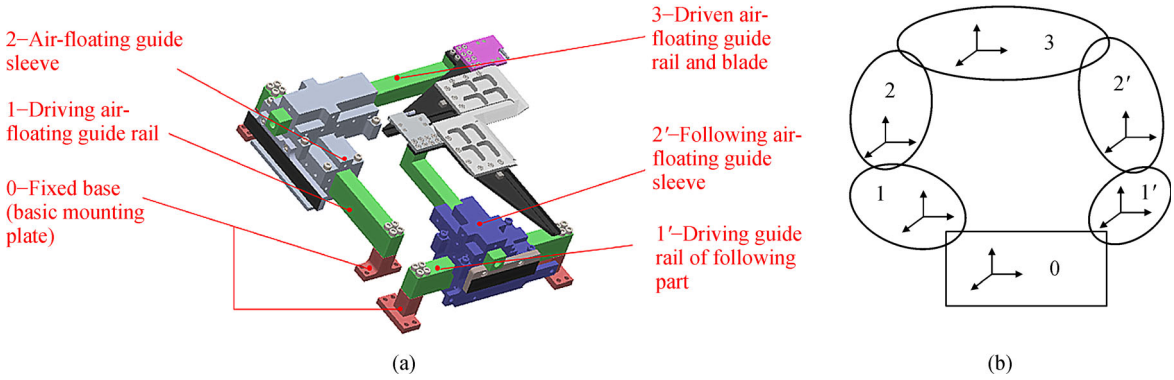

Fig. 7 Schematic illustrations of (a) the motion module structure of single blade and (b) its topology.

output module consists of a fixed base (basic mounting plate), driving air-floating guide rail, air-floating guide sleeve, driven air-floating guide rail, blade, following air-floating guide sleeve, and driving guide rail of the following part. The topology is shown in Fig. 7(b).

The geometric motion model of the HSVSS can be established according to its topology, and motion errors can be substituted into the model. First, the basic mounting plate coordinate system CS_0, the driving air-floating guide rail coordinate system CS_1, the air-floating guide sleeve coordinate system CS_2, the driven air-floating guide rail and blade coordinate system CS_3, the driving guide rail of following part $CS_{1'}$, and the following air-floating guide sleeve coordinate system $CS_{2'}$ are established. Then the transfer characteristic matrixes are established under ideal conditions and actual conditions. The transfer characteristic matrix represents the coordinate transformation between adjacent rigid bodies. Information on the position of the blade in the basic mounting plate coordinate system under ideal conditions and actual conditions can be expressed, and an expression for the blade position error can be obtained.

As shown in Fig. 8, rigid bodies B_1, B_2, …, B_k, B_{k+1} are in ideal positions $B_{1\text{-ideal}}$, $B_{2\text{-ideal}}$, …, $B_{k\text{-ideal}}$, $B_{k+1\text{-ideal}}$, respectively, under ideal conditions. Due to motion errors, rigid bodies B_1, B_2, …, B_k, B_{k+1} are in real positions $B_{1\text{-real}}$, $B_{2\text{-real}}$, …, $B_{k\text{-real}}$, $B_{k+1\text{-real}}$ under real conditions. The ideal coordinate transformation matrix is defined as ${}^{i}\boldsymbol{T}_{k}^{k+1}$ and the error matrix is defined as ${}^{e}\boldsymbol{T}_{k}^{k+1}$. The coordinate transformation matrixes, error matrixes in the HSVSS and types of errors between adjacent rigid bodies are shown in Tables 2 and 3.

Coordinate (x_s, y_s, z_s) denotes the origin of each part in the low-order body coordinate system in the static state. The relationships for converting between the coordinate systems are 0-1 (CS_0-CS_1), 1-2 (CS_1-CS_2), 2-3 (CS_2-CS_3), 0-1′ (CS_0-$CS_{1'}$), 1′-2′ ($CS_{1'}$-$CS_{2'}$), and 2′-3 ($CS_{2'}$-CS_3). The ideal position coordinate of point P on the blade in the basic mounting plate coordinate system is obtained by ideal coordinate transformation matrixes and it is expressed as:

$$P_{\text{ideal}} = {}^{i}\boldsymbol{T}_{0}^{1}\ {}^{i}\boldsymbol{T}_{1}^{2}\ {}^{i}\boldsymbol{T}_{2}^{3}[x_p, y_p, z_p, 1]^{\mathrm{T}}. \tag{1}$$

Due to errors, the position coordinate of point P on the blade in the basic mounting plate coordinate system under actual conditions is obtained by ideal coordinate transformation matrixes and actual coordinate transformation matrixes. Based on geometric motion model of the HSVSS, the actual position of the blade is affected by the air-floating rail to which it belongs and the following blade that it is connected to. As shown in Fig. 7(b), 0-1-2-3

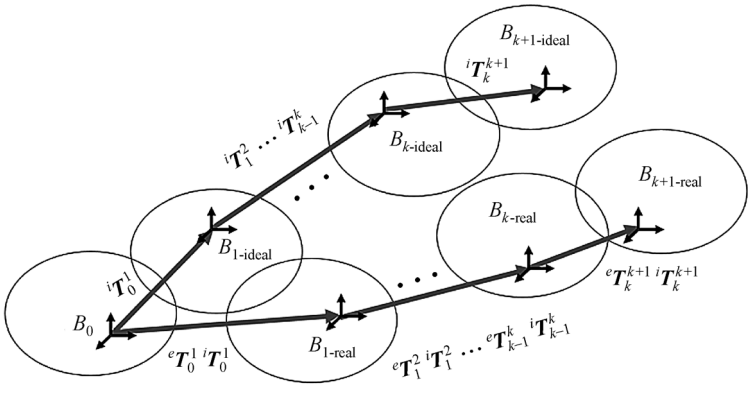

Fig. 8 Error description of adjacent rigid bodies.

Table 2 Coordinate transformation matrices and error matrices of blade moving along the Y direction (unit: m)

Adjacent rigid body	Coordinate transformation matrix under ideal condition	Error matrix	Type of error
0-1	${}^{i}\boldsymbol{T}_{0}^{1}=\begin{bmatrix}1&0&0&x_{\mathrm{s}}\\0&1&0&y_{\mathrm{s}}\\0&0&1&z_{\mathrm{s}}\\0&0&0&1\end{bmatrix}$	${}^{e}\boldsymbol{T}_{0}^{1}=\begin{bmatrix}1&-\delta Rz_{0\text{-}1}&\delta Ry_{0\text{-}1}&\delta x_{0\text{-}1}\\\delta Rz_{0\text{-}1}&1&-\delta Rx_{0\text{-}1}&\delta y_{0\text{-}1}\\-\delta Ry_{0\text{-}1}&\delta Rx_{0\text{-}1}&1&\delta z_{0\text{-}1}\\0&0&0&1\end{bmatrix}$	Assembly error
1-2	${}^{i}\boldsymbol{T}_{1}^{2}=\begin{bmatrix}1&0&0&x_{\mathrm{s}}\\0&1&0&y_{\mathrm{s}}+y\\0&0&1&z_{\mathrm{s}}\\0&0&0&1\end{bmatrix}$	${}^{e}\boldsymbol{T}_{1}^{2}=\begin{bmatrix}1&-\delta Rz_{1\text{-}2}&\delta Ry_{1\text{-}2}&\delta x_{1\text{-}2}\\\delta Rz_{1\text{-}2}&1&-\delta Rx_{1\text{-}2}&\delta y_{1\text{-}2}\\-\delta Ry_{1\text{-}2}&\delta Rx_{1\text{-}2}&1&\delta z_{1\text{-}2}\\0&0&0&1\end{bmatrix}$	Measurement error, dynamic error, and straightness error
2-3	${}^{i}\boldsymbol{T}_{2}^{3}=\begin{bmatrix}1&0&0&x_{\mathrm{s}}+x\\0&1&0&y_{\mathrm{s}}\\0&0&1&z_{\mathrm{s}}\\0&0&0&1\end{bmatrix}$	${}^{e}\boldsymbol{T}_{2}^{3}=\begin{bmatrix}1&-\delta Rz_{2\text{-}3}&\delta Ry_{2\text{-}3}&\delta x_{2\text{-}3}\\\delta Rz_{2\text{-}3}&1&-\delta Rx_{2\text{-}3}&\delta y_{2\text{-}3}\\-\delta Ry_{2\text{-}3}&\delta Rx_{2\text{-}3}&1&\delta z_{2\text{-}3}\\0&0&0&1\end{bmatrix}$	Assembly error, straightness error, dynamic error, and thermal error
0-1′	${}^{i}\boldsymbol{T}_{0}^{1'}=\begin{bmatrix}1&0&0&x_{\mathrm{s}}\\0&1&0&y_{\mathrm{s}}\\0&0&1&z_{\mathrm{s}}\\0&0&0&1\end{bmatrix}$	${}^{e}\boldsymbol{T}_{0}^{1'}=\begin{bmatrix}1&-\delta Rz_{0\text{-}1'}&\delta Ry_{0\text{-}1'}&\delta x_{0\text{-}1'}\\\delta Rz_{0\text{-}1'}&1&-\delta Rx_{0\text{-}1'}&\delta y_{0\text{-}1'}\\-\delta Ry_{0\text{-}1'}&\delta Rx_{0\text{-}1'}&1&\delta z_{0\text{-}1'}\\0&0&0&1\end{bmatrix}$	Assembly error
1′-2′	${}^{i}\boldsymbol{T}_{1'}^{2'}=\begin{bmatrix}1&0&0&x_{\mathrm{s}}+x\\0&1&0&y_{\mathrm{s}}\\0&0&1&z_{\mathrm{s}}\\0&0&0&1\end{bmatrix}$	${}^{e}\boldsymbol{T}_{1'}^{2'}=\begin{bmatrix}1&-\delta Rz_{1'\text{-}2'}&\delta Ry_{1'\text{-}2'}&\delta x_{1'\text{-}2'}\\\delta Rz_{1'\text{-}2'}&1&-\delta Rx_{1'\text{-}2'}&\delta y_{1'\text{-}2'}\\-\delta Ry_{1'\text{-}2'}&\delta Rx_{1'\text{-}2'}&1&\delta z_{1'\text{-}2'}\\0&0&0&1\end{bmatrix}$	Straightness error
2′-3	$\boldsymbol{T}_{2'}^{3}=\begin{bmatrix}1&0&0&x_{\mathrm{s}}\\0&1&0&y_{\mathrm{s}}+y\\0&0&1&z_{\mathrm{s}}\\0&0&0&1\end{bmatrix}$	${}^{e}\boldsymbol{T}_{2'}^{3}=\begin{bmatrix}1&-\delta Rz_{2'\text{-}3}&\delta Ry_{2'\text{-}3}&\delta x_{2'\text{-}3}\\\delta Rz_{2'\text{-}3}&1&-\delta Rx_{2'\text{-}3}&\delta y_{2'\text{-}3}\\-\delta Ry_{2'\text{-}3}&\delta Rx_{2'\text{-}3}&1&\delta z_{2'\text{-}3}\\0&0&0&1\end{bmatrix}$	Assembly error and straightness error

(CS_0-CS_1-CS_2-CS_3) and 0-1′-2′-3 (CS_0-$CS_{1'}$-$CS_{2'}$-CS_3) are two separate coordinate transfer chains. The influences of geometric errors from two coordinate transfer chains on the actual position of point P are independent of each other. Therefore, the actual position coordinate of point P can be expressed as

$$P_{\mathrm{real}}={}^{e}\boldsymbol{T}_{0}^{1}\,{}^{i}\boldsymbol{T}_{0}^{1}\,{}^{e}\boldsymbol{T}_{1}^{2}\,{}^{i}\boldsymbol{T}_{1}^{2}\,{}^{e}\boldsymbol{T}_{2}^{3}\,{}^{i}\boldsymbol{T}_{2}^{3}[x_{\mathrm{p}},y_{\mathrm{p}},z_{\mathrm{p}},1]^{\mathrm{T}}+{}^{e}\boldsymbol{T}_{0}^{1'}\,{}^{i}\boldsymbol{T}_{0}^{1'}\,{}^{e}\boldsymbol{T}_{1'}^{2'}\,{}^{i}\boldsymbol{T}_{1'}^{2'}\,{}^{e}\boldsymbol{T}_{2'}^{3}\,{}^{i}\boldsymbol{T}_{2}^{3}[x_{\mathrm{p}},y_{\mathrm{p}},z_{\mathrm{p}},1]^{\mathrm{T}}. \quad (2)$$

The position error of point P on the blade in the basic mounting plate coordinate system is

$$\Delta P=P_{\mathrm{real}}-P_{\mathrm{ideal}}. \quad (3)$$

3.2 Analysis of influence of error sources on the displacement error

The influence coefficient of the error sources on the displacement error of the blade can be obtained by taking the partial derivative of each error term with respect to $\Delta P=[\Delta x_i,\Delta y_i,\Delta z_i,0]^{\mathrm{T}}$, as follows:

$$K_{x_i}(\delta_j)=\frac{\partial\Delta x_i}{\partial\delta_j}, \quad (4)$$

$$K_{y_i}(\delta_j)=\frac{\partial\Delta y_i}{\partial\delta_j}, \quad (5)$$

Table 3 Coordinate transformation matrices and error matrices of blade moving along the X direction (unit: m)

Adjacent rigid body	Coordinate transformation matrix under ideal condition	Error matrix	Types of error
0-1	${}^{i}\boldsymbol{T}_{0}^{1}=\begin{bmatrix}1&0&0&x_s\\0&1&0&y_s\\0&0&1&z_s\\0&0&0&1\end{bmatrix}$	${}^{e}\boldsymbol{T}_{0}^{1}=\begin{bmatrix}1&-\delta Rz_{0\text{-}1}&\delta Ry_{0\text{-}1}&\delta x_{0\text{-}1}\\\delta Rz_{0\text{-}1}&1&-\delta Rx_{0\text{-}1}&\delta y_{0\text{-}1}\\-\delta Ry_{0\text{-}1}&\delta Rx_{0\text{-}1}&1&\delta z_{0\text{-}1}\\0&0&0&1\end{bmatrix}$	Assembly error
1-2	${}^{i}\boldsymbol{T}_{1}^{2}=\begin{bmatrix}1&0&0&x_s+x\\0&1&0&y_s\\0&0&1&z_s\\0&0&0&1\end{bmatrix}$	${}^{e}\boldsymbol{T}_{1}^{2}=\begin{bmatrix}1&-\delta Rz_{1\text{-}2}&\delta Ry_{1\text{-}2}&\delta x_{1\text{-}2}\\\delta Rz_{1\text{-}2}&1&-\delta Rx_{1\text{-}2}&\delta y_{1\text{-}2}\\-\delta Ry_{1\text{-}2}&\delta Rx_{1\text{-}2}&1&\delta z_{1\text{-}2}\\0&0&0&1\end{bmatrix}$	Measurement error and straightness error
2-3	${}^{i}\boldsymbol{T}_{2}^{3}=\begin{bmatrix}1&0&0&x_s\\0&1&0&y_s+y\\0&0&1&z_s\\0&0&0&1\end{bmatrix}$	${}^{e}\boldsymbol{T}_{2}^{3}=\begin{bmatrix}1&-\delta Rz_{2\text{-}3}&\delta Ry_{2\text{-}3}&\delta x_{2\text{-}3}\\\delta Rz_{2\text{-}3}&1&-\delta Rx_{2\text{-}3}&\delta y_{2\text{-}3}\\-\delta Ry_{2\text{-}3}&\delta Rx_{2\text{-}3}&1&\delta z_{2\text{-}3}\\0&0&0&1\end{bmatrix}$	Assembly error, straightness error, and thermal error
0-1′	${}^{i}\boldsymbol{T}_{0}^{1'}=\begin{bmatrix}1&0&0&x_s\\0&1&0&y_s\\0&0&1&z_s\\0&0&0&1\end{bmatrix}$	${}^{e}\boldsymbol{T}_{0}^{1'}=\begin{bmatrix}1&-\delta Rz_{0\text{-}1'}&\delta Ry_{0\text{-}1'}&\delta x_{0\text{-}1'}\\\delta Rz_{0\text{-}1'}&1&-\delta Rx_{0\text{-}1'}&\delta y_{0\text{-}1'}\\-\delta Ry_{0\text{-}1'}&\delta Rx_{0\text{-}1'}&1&\delta z_{0\text{-}1'}\\0&0&0&1\end{bmatrix}$	Assembly error
1′-2′	${}^{i}\boldsymbol{T}_{1'}^{2'}=\begin{bmatrix}1&0&0&x_s\\0&1&0&y_s+y\\0&0&1&z_s\\0&0&0&1\end{bmatrix}$	${}^{e}\boldsymbol{T}_{1'}^{2'}=\begin{bmatrix}1&-\delta Rz_{1'\text{-}2'}&\delta Ry_{1'\text{-}2'}&\delta x_{1'\text{-}2'}\\\delta Rz_{1'\text{-}2'}&1&-\delta Rx_{1'\text{-}2'}&\delta y_{1'\text{-}2'}\\-\delta Ry_{1'\text{-}2'}&\delta Rx_{1'\text{-}2'}&1&\delta z_{1'\text{-}2'}\\0&0&0&1\end{bmatrix}$	Straightness error
2′-3	$\boldsymbol{T}_{2'}^{3}=\begin{bmatrix}1&0&0&x_s+x\\0&1&0&y_s\\0&0&1&z_s\\0&0&0&1\end{bmatrix}$	${}^{e}\boldsymbol{T}_{2'}^{3}=\begin{bmatrix}1&-\delta Rz_{2'\text{-}3}&\delta Ry_{2'\text{-}3}&\delta x_{2'\text{-}3}\\\delta Rz_{2'\text{-}3}&1&-\delta Rx_{2'\text{-}3}&\delta y_{2'\text{-}3}\\-\delta Ry_{2'\text{-}3}&\delta Rx_{2'\text{-}3}&1&\delta z_{2'\text{-}3}\\0&0&0&1\end{bmatrix}$	Assembly error and straightness error

$$K_{z_i}(\delta_j)=\frac{\partial \Delta z_i}{\partial \delta_j}, \tag{6}$$

where i represents X1, X2, Y1, and Y2, and δ_j represents the jth error source.

The optical axis of the optical system is set as origin of the coordinate system. The travel range of blade moving along X direction is ±22 mm and it can be expressed on the X-axis as [–0.022 m, 0.022 m]. The travel range of blade moving along Y direction is ±30 mm and it can be expressed on the Y-axis as [–0.030 m, 0.030 m]. The maximum window formed by four blades is 28 mm in the X direction and 20 mm in the Y direction during the blade scanning process. The window is shown in Fig. 9(a), and point P is the center point of the window. The influence coefficient of error sources on the displacement error of the blade is different when the blade is in different positions. Therefore, the influence coefficient of error sources is analyzed when the window formed by blades is at different positions in this paper. Nine points P_1–P_9 are taken and their positions and their coordinates are shown in Fig. 9(b). These nine points are different positions of the window center. When the window center is at P_1, P_2 or P_3, Blade Y1 is at the top of its travel range; when the window center is at P_7, P_8 or P_9, Blade Y2 is at the bottom of its travel range; when the window center is at P_1, P_4 or P_7, Blade X2 is at the leftmost end of its travel range; and when the window center is at P_3, P_6 or P_9, Blade X1 is at the rightmost end of its travel range.

The coordinate transformation matrixes under ideal condition and error matrixes of four blades are shown in Table 4, and the values of matrixes are shown in Table 5.

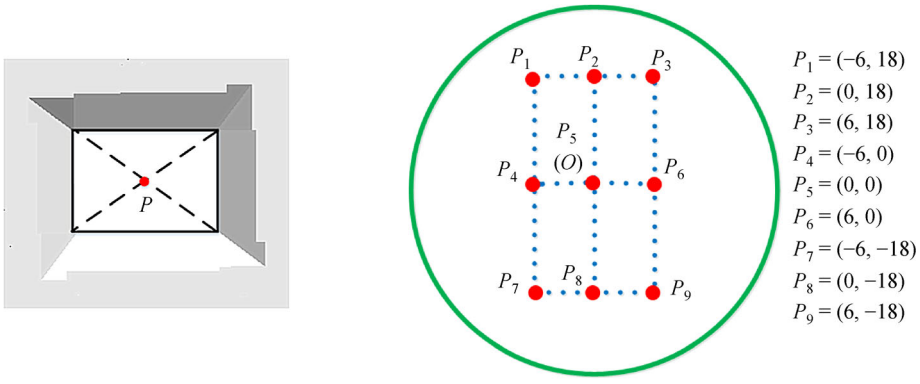

(a) (b)

Fig. 9 (a) Definition and (b) positions of window center.

Table 4 Coordinate transformation matrices and error matrices of blade (unit: m)

Adjacent rigid bodies	Coordinate transformation matrix under ideal condition	Error matrix
0-1	$^{i}\boldsymbol{T}_{0}^{1}=\begin{bmatrix}1&0&0&l_{x0}\\0&1&0&l_{y0}\\0&0&1&l_{z0}\\0&0&0&1\end{bmatrix}$	$^{e}\boldsymbol{T}_{0}^{1}=\begin{bmatrix}1&-\delta Rz_{0\text{-}1}&\delta Ry_{0\text{-}1}&\delta x_{0\text{-}1}\\\delta Rz_{0\text{-}1}&1&-\delta Rx_{0\text{-}1}&\delta y_{0\text{-}1}\\-\delta Ry_{0\text{-}1}&\delta Rx_{0\text{-}1}&1&\delta z_{0\text{-}1}\\0&0&0&1\end{bmatrix}$
1-2	$^{i}\boldsymbol{T}_{1}^{2}=\begin{bmatrix}1&0&0&l_{x1}\\0&1&0&l_{y1}\\0&0&1&l_{z1}\\0&0&0&1\end{bmatrix}$	$^{e}\boldsymbol{T}_{1}^{2}=\begin{bmatrix}1&-\delta Rz_{1\text{-}2}&\delta Ry_{1\text{-}2}&\delta x_{1\text{-}2}\\\delta Rz_{1\text{-}2}&1&-\delta Rx_{1\text{-}2}&\delta y_{1\text{-}2}\\-\delta Ry_{1\text{-}2}&\delta Rx_{1\text{-}2}&1&\delta z_{1\text{-}2}\\0&0&0&1\end{bmatrix}$
2-3	$^{i}\boldsymbol{T}_{1}^{2}=\begin{bmatrix}1&0&0&l_{x2}\\0&1&0&l_{y2}\\0&0&1&l_{z2}\\0&0&0&1\end{bmatrix}$	$^{e}\boldsymbol{T}_{2}^{3}=\begin{bmatrix}1&-\delta Rz_{2\text{-}3}&\delta Ry_{2\text{-}3}&\delta x_{2\text{-}3}\\\delta Rz_{2\text{-}3}&1&-\delta Rx_{2\text{-}3}&\delta y_{2\text{-}3}\\-\delta Ry_{2\text{-}3}&\delta Rx_{2\text{-}3}&1&\delta z_{2\text{-}3}\\0&0&0&1\end{bmatrix}$
0-1′	$^{i}\boldsymbol{T}_{0}^{1'}=\begin{bmatrix}1&0&0&l_{x0'}\\0&1&0&l_{y0'}\\0&0&1&l_{z0'}\\0&0&0&1\end{bmatrix}$	$^{e}\boldsymbol{T}_{0}^{1'}=\begin{bmatrix}1&-\delta Rz_{0\text{-}1'}&\delta Ry_{0\text{-}1'}&\delta x_{0\text{-}1'}\\\delta Rz_{0\text{-}1'}&1&-\delta Rx_{0\text{-}1'}&\delta y_{0\text{-}1'}\\-\delta Ry_{0\text{-}1'}&\delta Rx_{0\text{-}1'}&1&\delta z_{0\text{-}1'}\\0&0&0&1\end{bmatrix}$
1′-2′	$^{i}\boldsymbol{T}_{1'}^{2'}=\begin{bmatrix}1&0&0&l_{x1'}\\0&1&0&l_{y1'}\\0&0&1&l_{z1'}\\0&0&0&1\end{bmatrix}$	$^{e}\boldsymbol{T}_{1'}^{2'}=\begin{bmatrix}1&-\delta Rz_{1'\text{-}2'}&\delta Ry_{1'\text{-}2'}&\delta x_{1'\text{-}2'}\\\delta Rz_{1'\text{-}2'}&1&-\delta Rx_{1'\text{-}2'}&\delta y_{1'\text{-}2'}\\-\delta Ry_{1'\text{-}2'}&\delta Rx_{1'\text{-}2'}&1&\delta z_{1'\text{-}2'}\\0&0&0&1\end{bmatrix}$
2′-3	$^{i}\boldsymbol{T}_{2'}^{3}=\begin{bmatrix}1&0&0&l_{x2'}\\0&1&0&l_{y2'}\\0&0&1&l_{z2'}\\0&0&0&1\end{bmatrix}$	$^{e}\boldsymbol{T}_{2'}^{3}=\begin{bmatrix}1&-\delta Rz_{2'\text{-}3}&\delta Ry_{2'\text{-}3}&\delta x_{2'\text{-}3}\\\delta Rz_{2'\text{-}3}&1&-\delta Rx_{2'\text{-}3}&\delta y_{2'\text{-}3}\\-\delta Ry_{2'\text{-}3}&\delta Rx_{2'\text{-}3}&1&\delta z_{2'\text{-}3}\\0&0&0&1\end{bmatrix}$

Table 5 Values of coordinate transformation matrixes under ideal condition (unit: m)

Values of Blade Y1	Values of Blade Y2	Values of Blade X1	Values of Blade X2
$l_{x0} = 0.0205$	$l_{x0} = 0.2495$	$l_{x0} = 0.125$	$l_{x0} = 0.145$
$l_{y0} = 0.127$	$l_{y0} = 0.179$	$l_{y0} = 0.215$	$l_{y0} = 0.091$
$l_{z0} = 0.02955$	$l_{z0} = 0.02955$	$l_{z0} = 0.03195$	$l_{z0} = 0.03195$
$l_{x1} = 0$	$l_{x1} = 0$	$l_{x1} = 0.09792 + b$	$l_{x1} = -0.04991 + b$
$l_{y1} = 0.07342 + a$	$l_{y1} = -0.03741 + a$	$l_{y1} = 0$	$l_{y1} = 0$
$l_{z1} = 0$	$l_{z1} = 0$	$l_{z1} = 0$	$l_{z1} = 0$
$l_{z1} = -0.04395 + b$	$l_{z1} = 0.03195 + b$	$l_{z1} = -0.0165$	$l_{z1} = -0.0435$
$l_{y2} = 0.037$	$l_{y2} = -0.08041$	$l_{y2} = 0.05445 + a$	$l_{y2} = -0.01845 + a$
$l_{z2} = 0.027$	$l_{z2} = 0.027$	$l_{z2} = 0.026$	$l_{z2} = 0.026$
$l_{x0'} = 0.145$	$l_{x0'} = 0.125$	$l_{x0'} = 0.0205$	$l_{x0'} = 0.2495$
$l_{y0'} = 0.091$	$l_{y0'} = 0.215$	$l_{y0'} = 0.127$	$l_{y0'} = 0.179$
$l_{z0'} = 0.03195$	$l_{z0'} = 0.03195$	$l_{z0'} = 0.02955$	$l_{z0'} = 0.02955$
$l_{x1'} = -0.04991 + b$	$l_{x1'} = 0.09792 + b$	$l_{x1'} = 0$	$l_{x1'} = 0$
$l_{y1'} = 0$	$l_{y1'} = 0$	$l_{y1'} = 0.07342 + a$	$l_{y1'} = -0.03741 + a$
$l_{z1'} = 0$	$l_{z1'} = 0$	$l_{z1'} = 0$	$l_{z1'} = 0$
$l_{x2'} = -0.11854$	$l_{x2'} = 0.05853$	$l_{x2'} = 0.18592 + b$	$l_{x2'} = -0.19791 + b$
$l_{y2'} = 0.15242 + a$	$l_{y2'} = -0.11641 + a$	$l_{y2'} = 0.06903$	$l_{y2'} = -0.06904$
$l_{z2'} = 0.0246$	$l_{z2'} = 0.0246$	$l_{z2'} = 0.0284$	$l_{z2'} = 0.0284$

Parameters a and b in matrixes taking different values indicated that the center of the window is at to different points, and the corresponding relation is shown in Table 6. Point P on the blade is taken in the CS_3 coordinate system and the coordinate values of point P on the four blades are shown in Table 7.

Table 6 Values of a and b when the blade is at different positions

Position	a/m	b/m
P_1	0.000	0.000
P_2	–0.018	0.000
P_3	–0.036	0.000
P_4	0.000	0.006
P_5	–0.018	0.006
P_6	–0.036	0.006
P_7	0.000	0.012
P_8	–0.018	0.012
P_9	–0.036	0.012

Table 7 Coordinate values of the point P on the four blades in the CS_3 coordinate

Blade	Coordinate values/mm
Y1	(0.17284, –0.06242, 0.01955)
Y2	(0.06341, 0.11484, 0.01815)
X1	(–0.17284, 0.06242, 0.01955)
X2	(–0.06341, –0.11484, 0.01815)

According to Eq. (2), the actual position of point P on the blade in the basic mounting plate coordinate system can be calculated. According to Eq. (3), the deviation $\Delta P = [\Delta x, \Delta y, \Delta z, 0]^{\mathrm{T}}$ between the actual position and the ideal position of point P can be calculated. Finally, according to Eqs. (4)–(6), the influence coefficient of error sources of every error source in the error matrixes of the four blades at different positions on error components Δx, Δy, and Δz of ΔP are calculated, and bar graphs are made as shown in Figs. 10–13, where (a), (b), and (c) are influence coefficient diagrams of the Δx, Δy, and Δz, respectively. Numbers along x-axis in Figs. 10–13 indicate the window centers P_1–P_9. Numbers along y-axis indicates that Δx, Δy, and Δz are influenced by 36 error sources, respectively, and the numbers of error sources are 1 to 36, where

1–6: Offset errors between adjacent bodies along x-axis;

7–12: Offset errors between adjacent bodies along y-axis;

13–18: Offset errors between adjacent bodies along z-axis;

19–24: Rotation errors between adjacent bodies around x-axis;

25–30: Rotation errors between adjacent bodies around y-axis;

31–36: Rotation errors between adjacent bodies around z-axis.

Based on the calculations and Figs. 10–13, a number of conclusions can be drawn:

1) Offset errors have the greatest influence on the

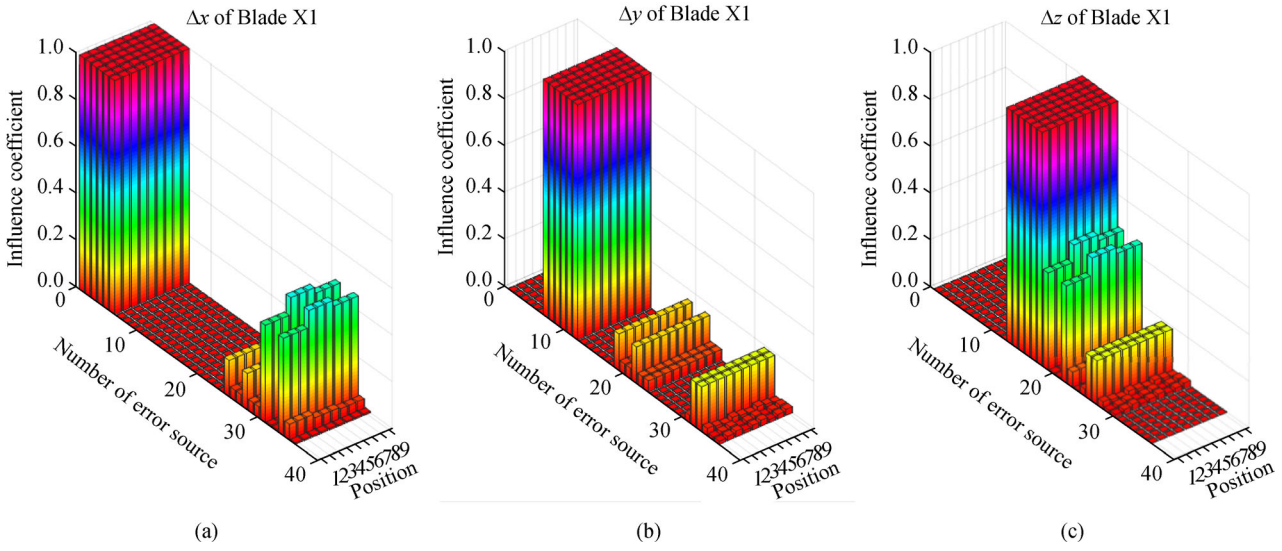

Fig. 10 The influence coefficient of error sources of Blade X1. (a) Δx of Blade X1; (b) Δy of Blade X1; (c) Δz of Blade X1.

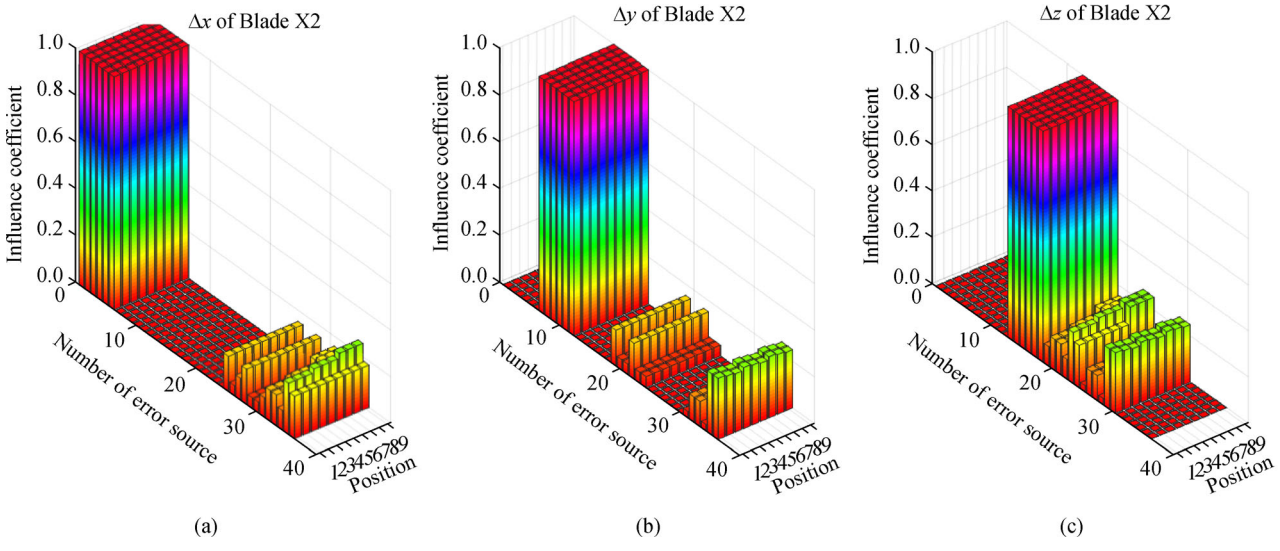

Fig. 11 The influence coefficient of error sources of Blade X2. (a) Δx of Blade X2; (b) Δy of Blade X2; (c) Δz of Blade X2.

displacement error. They are mainly caused by errors in the manufacture and assembly of HSVSS components.

2) Rotation errors in matrixes ${}^{e}\boldsymbol{T}_{0}^{1'}$ and ${}^{e}\boldsymbol{T}_{0}^{1}$ have a large influence on the displacement error and are mainly due to errors caused by installation of the driving air-floating guide rail.

3) Rotation errors in matrixes ${}^{e}\boldsymbol{T}_{2}^{3}$ and ${}^{e}\boldsymbol{T}_{2}^{3'}$ have little influence on the displacement error. They are due to errors caused by installation of the blades on the blade holders, installation of the air-floating guide sleeves, and movement of the driven air-floating guide rail.

4 Analysis of blade displacement error sources

When the blades are moving, the linear grating ruler can be used as a measurement feedback module to control the high-precision motion of the blades. Motion errors of the blades can be divided into errors obtained using the measurement feedback module and terrors from the motion module. Error is expressed in the form of a six-degree-of-freedom error vector $\left[\delta_x,\ \delta_y,\ \delta_z,\ \delta R_x,\ \delta R_y,\ \delta R_z\right]$, where δ_x, δ_y, and δ_z represent the offset error in the X, Y, and Z

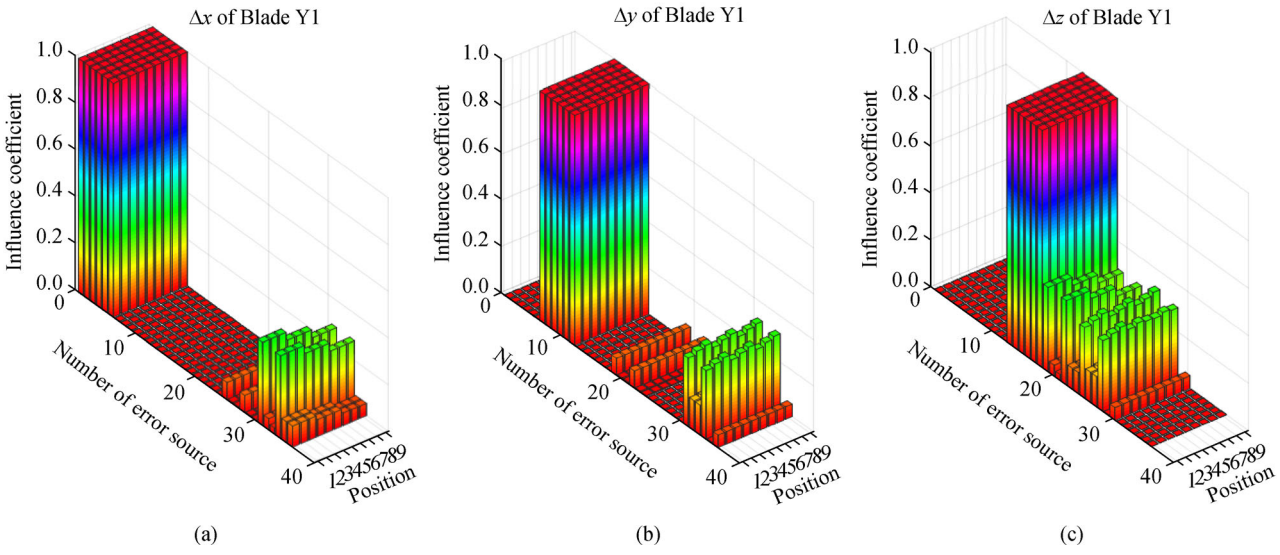

Fig. 12 The influence coefficient of error sources of Blade Y1. (a) Δx of Blade Y1; (b) Δy of Blade Y1; (c) Δz of Blade Y1.

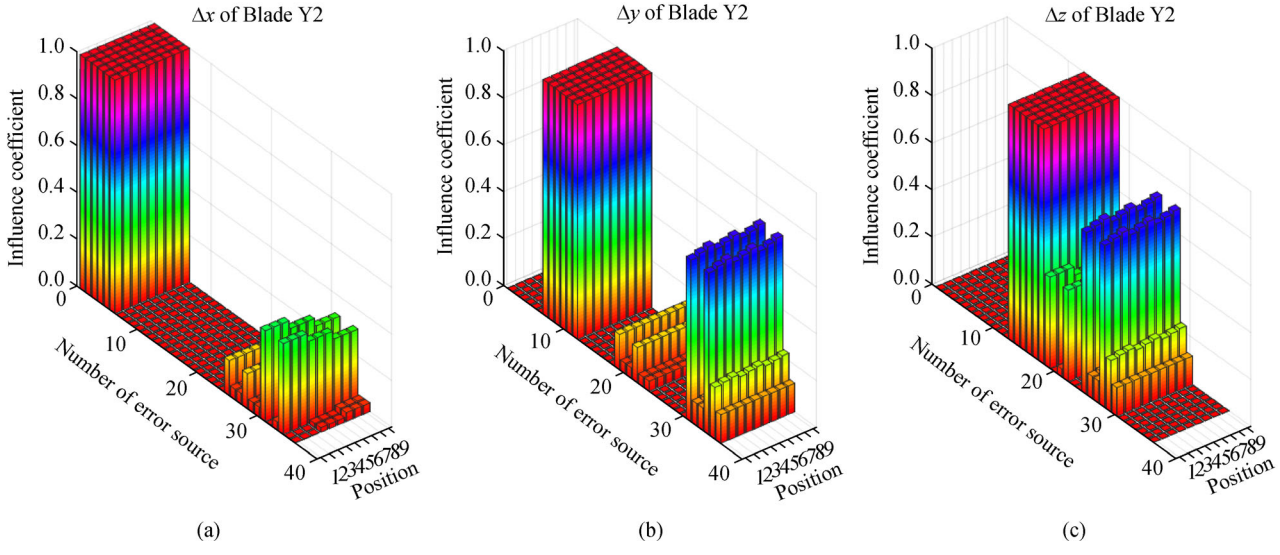

Fig. 13 The influence coefficient of error sources of Blade Y2. (a) Δx of Blade Y2; (b) Δy of Blade Y2; (c) Δz of Blade Y2.

directions, respectively, and δR_x, δR_y, and δR_z represent the rotation error in X, Y, and Z directions, respectively.

4.1 Measurement feedback module error

Errors obtained by the measurement feedback module include the assembly error, thermal error, and measurement error.

4.1.1 Assembly error

When the linear grating ruler is not parallel to the axis of the driving rail due to assembly errors, error will exist between the measurement result and the actual position of the measured object, as shown in Fig. 14.

Taking the blade moving along Y direction as an example and the length of the linear grating ruler as 100 mm, the cosine errors caused by the assembly error of linear grating ruler are

$$\delta y_{y1x} = L_{Y1} - L'_{Y1} = L_{Y1}(1-\cos\theta_{x1}) = 0.5L_{Y1}\theta_{x1}^2, \quad (7)$$

$$\delta y_{y1z} = L_{Y1} - L'_{Y1} = L_{Y1}(1-\cos\theta_{z1}) = 0.5L_{Y1}\theta_{z1}^2. \quad (8)$$

Maximum allowable errors of θ_{x1} and θ_{z1} are both 0.1 mrad. The maximal error caused by θ_{x1} and θ_{z1} are

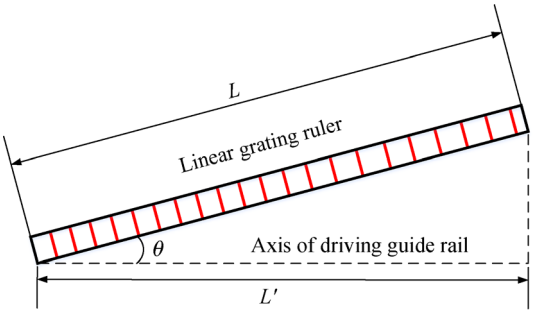

Fig. 14 Schematic of assembly errors of linear grating ruler.

$$\delta y_{yx} = 0.5 L_Y \theta_x^2 = 0.5 \times 0.1 \times (0.0001)^2 = 0.5 \text{ nm}, \quad (9)$$

$$\delta y_{yz} = 0.5 L_Y \theta_z^2 = 0.5 \times 0.1 \times (0.0001)^2 = 0.5 \text{ nm}. \quad (10)$$

The maximum assembly error of the blade moving along the Y direction can be determined by summing δy_{yx} and δy_{yz}, expressed as

$$\boldsymbol{\delta}_{1\_y} = [0,\ 0.001\ \mu\text{m},\ 0,\ 0,\ 0,\ 0]. \quad (11)$$

Similarly, the maximum assembly error of the blade moving along X direction can be obtained. The length of the linear grating ruler along the X direction is 80 mm, therefore, the maximum assembly error can be expressed as

$$\boldsymbol{\delta}_{1\_x} = [0.0008\ \mu\text{m},\ 0,\ 0,\ 0,\ 0,\ 0]. \quad (12)$$

4.1.2 Thermal error

The linear grating ruler used in this system is made of steel with a thermal expansion coefficient $\alpha_{\text{therm}} = 10^{-5}$ K^{-1}. Changes in temperature can cause variation in the grating period constant:

$$\Delta d = d\alpha_{\text{therm}}(t - t_0). \quad (13)$$

The measurement error introduced in the total range is

$$\delta_2 = N\Delta d. \quad (14)$$

Ambient temperature of the HSVSS is 22 °C. According to the simulation results, the maximum temperature of the motor coil moving along the X direction is 24 °C and the maximum temperature of the motor coil moving along the Y direction is 28 °C. The temperature of the linear grating ruler is the same as the temperature of the motor coil. The length of the linear grating ruler along the X direction is 80 mm and the length of linear grating ruler along the Y direction is 100 mm. The maximum thermal errors can be expressed as

$$\boldsymbol{\delta}_{2\_x} = [1.6\ \mu\text{m},\ 0,\ 0,\ 0,\ 0,\ 0], \quad (15)$$

$$\boldsymbol{\delta}_{2\_y} = [0,\ 6\ \mu\text{m},\ 0,\ 0,\ 0,\ 0]. \quad (16)$$

4.1.3 Measurement error

A laser interferometer can be used as a calibration tool. As the blade moves, measurements are obtained using the linear grating ruler and compared to those taken by the interferometer. The maximum measurement errors can be obtained as the maximum difference between the two measurements. The results are presented in Fig. 15. The maximum measurement error of the linear grating ruler along the X direction is 1.1 μm and the maximum measurement error of the linear grating ruler along Y direction is 1.5 μm, expressed as

$$\boldsymbol{\delta}_{3\_x} = [1.1\ \mu\text{m},\ 0,\ 0,\ 0,\ 0,\ 0], \quad (17)$$

$$\boldsymbol{\delta}_{3\_y} = [0,\ 1.5\ \mu\text{m},\ 0,\ 0,\ 0,\ 0]. \quad (18)$$

Assembly error, thermal error, and measurement error are all in the same coordinate system, therefore, no coordinate transformation is required. The total error obtained by the measurement feedback module δ_{m} is

$$\delta_{\text{m}} = \delta_1 + \delta_2 + \delta_3. \quad (19)$$

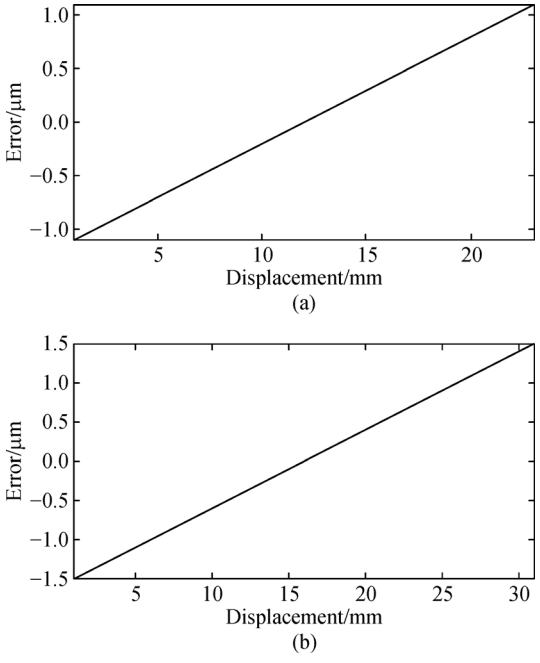

Fig. 15 Measurement error of the linear grating ruler along the (a) X and (b) Y directions, respectively.

4.2 Motion module error

4.2.1 Assembly error of driving guide rail

Geometric error of the driving air-floating guide rail is mainly caused by assembly errors, as shown in Fig. 16. The offset of the guide rail center of mass from the ideal position is expressed as the offset error of the rail, and the angle between the rail edge and the ideal axis is the angular error. The maximum assembly errors can be expressed as follows:

$$\boldsymbol{\delta}_{\text{fab\_}x1} = [3\ \mu\text{m},\ 3\ \mu\text{m},\ 0,\ 0,\ 0.018\ \mu\text{rad},\ 0.018\ \mu\text{rad}], \tag{20}$$

$$\boldsymbol{\delta}_{\text{fab\_}x2} = [3\ \mu\text{m},\ 3\ \mu\text{m},\ 0,\ 0,\ 0.018\ \mu\text{rad},\ 0.018\ \mu\text{rad}], \tag{21}$$

$$\boldsymbol{\delta}_{\text{fab\_}y1} = [3\ \mu\text{m},\ 3\ \mu\text{m},\ 0,\ 0.017\ \mu\text{rad},\ 0,\ 0.017\ \mu\text{rad}], \tag{22}$$

$$\boldsymbol{\delta}_{\text{fab\_}y2} = [3\ \mu\text{m},\ 3\ \mu\text{m},\ 0,\ 0.017\ \mu\text{rad},\ 0,\ 0.017\ \mu\text{rad}]. \tag{23}$$

4.2.2 Guide sleeve error

Error of guide sleeve of the two-dimensional double-layer orthogonal air-floating guide rail is comprised of the assembly error, straightness error of the guide rail, and thermal error.

4.2.2.1 Assembly error

Owing to assembly errors of the two-dimensional double-layer orthogonal air-floating guide rail, the driven guide rail may not be perpendicular to the driving guide rail. The maximum verticality error of the two-dimensional double-layer orthogonal air-floating guide rail can be measured by three coordinate machines: the verticality error of the air-floating sleeve carrying Blade X1 is 1.4 μm; the verticality error of the air-floating sleeve carrying Blade X2 is 1.5 μm; the verticality error of the air-floating sleeve carrying Blade Y1 is 2.3 μm; the verticality error of the air-floating sleeve carrying Blade Y2 is 2.5 μm.

As shown in Fig. 17, rotation error about the Z-axis of the driven guide rail is caused by verticality error. The relationship between the rotation error and verticality error is

$$\delta_{\text{par\_rot}} = \frac{\delta_{\text{par}}}{l}. \tag{24}$$

In the two-dimensional double-layer orthogonal air-floating guide rails carrying Blades X1 and X2, $l = 33$ mm. In the two-dimensional double-layer orthogonal air-floating guide rails carrying Blades Y1 and Y2, $l = 33$ mm. The rotation errors were calculated as

$$\boldsymbol{\delta}_{\text{par\_}x1} = [0,\ 0,\ 0,\ 0,\ 0,\ 0.042\ \mu\text{rad}], \tag{25}$$

$$\boldsymbol{\delta}_{\text{par\_}x2} = [0,\ 0,\ 0,\ 0,\ 0,\ 0.045\ \mu\text{rad}], \tag{26}$$

$$\boldsymbol{\delta}_{\text{par\_}y1} = [0,\ 0,\ 0,\ 0,\ 0,\ 0.053\ \mu\text{rad}], \tag{27}$$

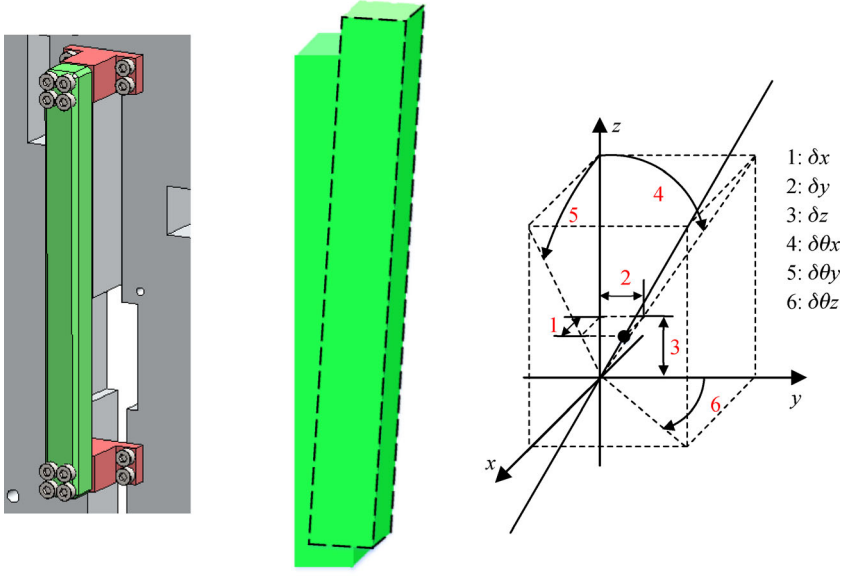

Fig. 16 Schematic illustration of the driving guide rail assembly error.

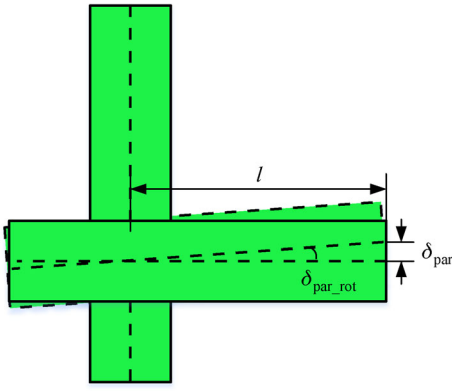

Fig. 17 Schematic drawing of rotation error caused by verticality error.

$$\boldsymbol{\delta}_{\text{par}\_y2} = [0,\ 0,\ 0,\ 0,\ 0,\ 0.058\ \mu\text{rad}]. \tag{28}$$

4.2.2.2 Straightness error

The straightness error of the air-floating guide rail can be measured using an autocollimator, and the experimental setup is shown in Fig. 18. The measuring rail, shown in Fig. 18, is the driving rail and belongs to the air-floating guide rail carrying Blade X2. Results presented in Fig. 19 were obtained by collating measurements.

The black straight lines in Fig. 19 are obtained by performing a least square fit on the obtained data. The straightness error can be obtained by the difference between experimental data and fitted straight line and it can be expressed as:

$$\delta_{\text{str}} = d_{\max} - d_{\min}. \tag{29}$$

According to the data, the straightness error along Z direction is 0.007 μm and the straightness error along Y direction is 0.003 μm.

$$\boldsymbol{\delta}_{\text{str}\_x2\_1} = [0,\ 0.003\ \mu\text{m},\ 0.007\ \mu\text{m},\ 0,\ 0,\ 0]. \tag{30}$$

Straightness errors of other guide rails were obtained using the same method and the following values were obtained:

$$\boldsymbol{\delta}_{\text{str}\_x2\_2} = [0.003\ \mu\text{m},\ 0,\ 0.007\ \mu\text{m},\ 0,\ 0,\ 0], \tag{31}$$

$$\boldsymbol{\delta}_{\text{str}\_x1\_1} = [0,\ 0.004\ \mu\text{m},\ 0.006\ \mu\text{m},\ 0,\ 0,\ 0], \tag{32}$$

$$\boldsymbol{\delta}_{\text{str}\_x1\_2} = [0.005\ \mu\text{m},\ 0,\ 0.007\ \mu\text{m},\ 0,\ 0,\ 0], \tag{33}$$

$$\boldsymbol{\delta}_{\text{str}\_y1\_1} = [0.008\ \mu\text{m},\ 0,\ 0.007\ \mu\text{m},\ 0,\ 0,\ 0], \tag{34}$$

$$\boldsymbol{\delta}_{\text{str}\_y1\_2} = [0,\ 0.008\ \mu\text{m},\ 0.006\ \mu\text{m},\ 0,\ 0,\ 0], \tag{35}$$

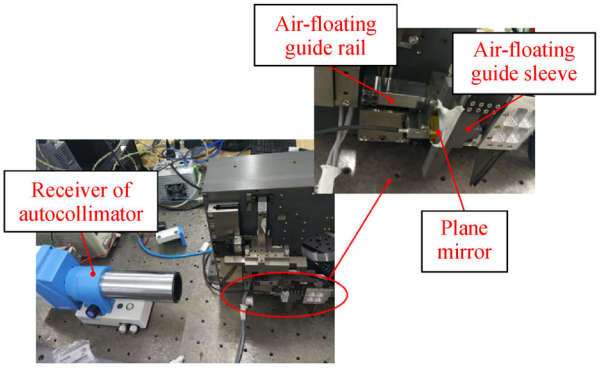

Fig. 18 Experimental setup for measuring the air-floating guide rail straightness.

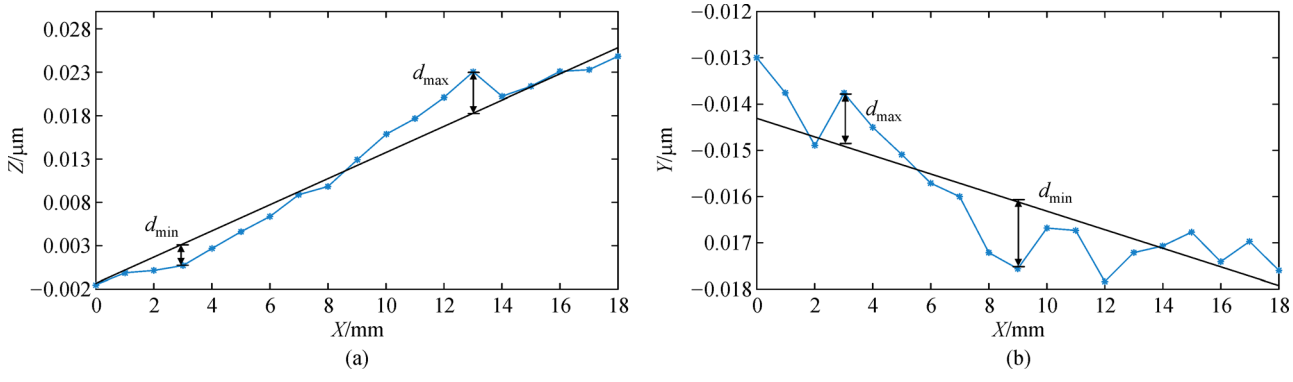

Fig. 19 Straightness error along the (a) Z and (b) Y directions when the guide rail is moving along the X direction, respectively.

$$\boldsymbol{\delta}_{\text{str\_}y2\_1} = [0.006\ \mu\text{m},\ 0,\ 0.007\ \mu\text{m},\ 0,\ 0,\ 0], \quad (36)$$

$$\boldsymbol{\delta}_{\text{str\_}y2\_2} = [0,\ 0.006\ \mu\text{m},\ 0.008\ \mu\text{m},\ 0,\ 0,\ 0]. \quad (37)$$

4.2.2.3 Thermal error

The expansive deformation of the air-floating sleeve after an increase in the temperature of the motor coil can be obtained using the finite element simulation method. In this case, the ambient temperature was 22 °C, the maximum temperature of the motor coil moving along Y direction was 28 °C, and the maximum temperature of the motor coil moving along X direction was 24 °C. Before the simulation, the temperature of the contact surface between the driving guide rail and the guide sleeve was the same as the ambient temperature.

The position error between driving guide rail and driven guide rail caused by the thermal deformation of guide sleeve can be expressed as

$$\boldsymbol{\delta}_{\text{therm\_}x} = [-0.002\ \mu\text{m},\ 0.082\ \mu\text{m},\ 0.023\ \mu\text{m},\ 0,\ 0,\ 0], \quad (38)$$

$$\boldsymbol{\delta}_{\text{therm\_}y} = [0.031\ \mu\text{m},\ 0.028\ \mu\text{m},\ 0.009\ \mu\text{m},\ 0,\ 0,\ 0]. \quad (39)$$

4.2.3 Dynamic error of scanning blade

4.2.3.1 Inertial force deformation error

During the acceleration of the scanning blade, the mechanism of deformation will be inertial forces, leading to deviation between the position of the blade and the position detected by the linear grating ruler. Simulation results are shown in Fig. 20. When the extension length of the driven guide rail is maximum, the maximum error is introduced by the scanning blade in the scanning direction due to inertial force deformation and is approximately 8.3 μm, expressed as

$$\boldsymbol{\delta}_{\text{inertia force}} = [0,\ 0,\ 8.3\ \mu\text{m},\ 0,\ 0,\ 0]. \quad (40)$$

4.2.3.2 Error caused by air gap variation

Because the center of mass of the moving part is not on the axis of the air-floating guide rail, an angle of deflection θ exists between the guide sleeve and the guide rail, and appears during acceleration and deceleration of the scanning blade, as shown in Fig. 21. The air gap between the guide sleeve and the guide rail can modeled as four elastic elements with a bearing capacity of W_1, W_2, W_3 and W_4, respectively, and the angular stiffness of the guide rail is $K_W(\theta)$. The relationship between deflection angle of the guide rail and bearing capacity is

$$\theta = \frac{(W_1 - W_2) - (W_3 - W_4)}{K_W(\theta)}. \quad (41)$$

The angular stiffness of the air-floating guide rail can be measured by experiment. The guide rail is placed vertically, and a load is added to one side of the guide sleeve. Height differences are measured when a load is added and removed from between two sides of the guide sleeve. The experimental data is presented in Table 8. The empty state means there is no load on the guide sleeve, and the full loaded state means the load required to deflect the guide rail at the maximum angle. When the guide rail was fully loaded, the torque was calculated to be 2.071 N·m and the distance between position A and position B in the table was 56 mm. The average of three measurements was calculated and the maximum deflection angle of the rail was calculated as 0.15 mrad.

When the driven guide rail had the longest extension length and the scanning blade moved with the maximum acceleration (10g, g: Gravitational acceleration), the torque

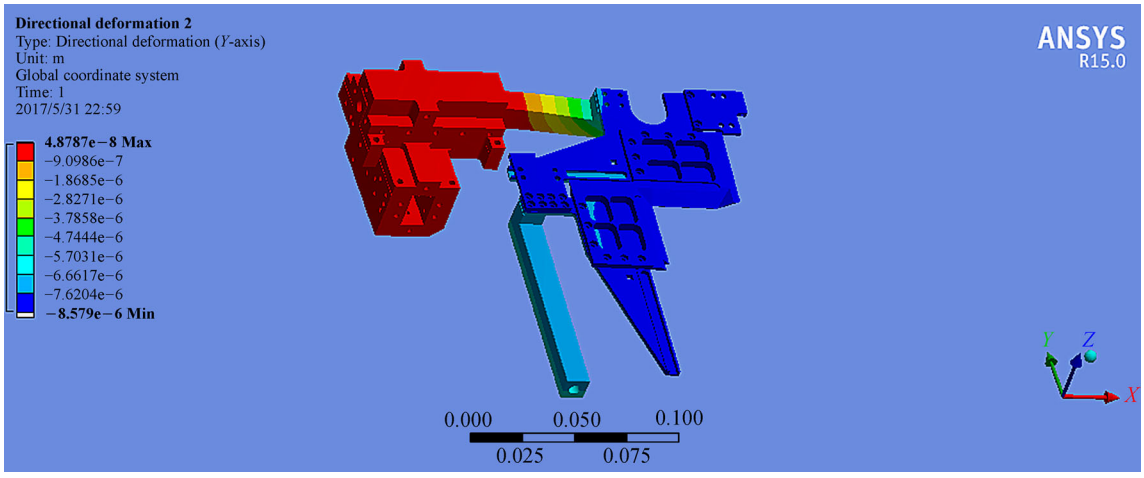

Fig. 20 Simulation results for the inertial force deformation.

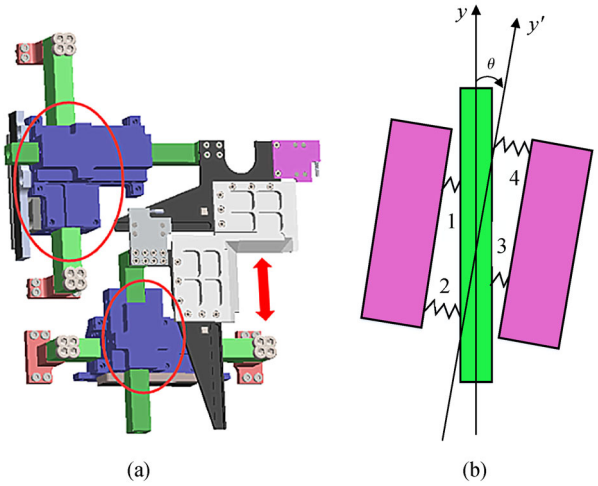

Fig. 21 Schematic of the air gap variation of air-floating guide rail. (a) Deflecting guide rail sleeves; (b) the elastic model of air-floating guide rail.

Table 8 Experiment data of angle stiffness of the guide rail (unit: mm)

Number	State	Position A	Position B	Height difference
1	Empty	105.6492	105.6526	–0.0034
	Full loaded	105.2295	105.2247	0.0048
2	Empty	105.5297	105.5340	–0.0043
	Full loaded	105.1969	105.1929	0.0044
3	Empty	105.5192	105.5231	–0.0039
	Full loaded	105.2017	105.1973	0.0044

was calculated as 1.86 N·m. The relationship between the torque and rotation angle was assumed to be linear in the deflection range of the guide rail, and the deflection angle of the guide rail was calculated to be 0.269 mrad. The maximum deflection error caused by the change in air gap due to acceleration or deceleration can be expressed as

$$\boldsymbol{\delta}_{\text{air\_gap}} = [0,\ 0,\ 0,\ 0,\ 0,\ 0.269\ \text{mrad}]. \tag{42}$$

5 Uncertainty evaluation

Measurement uncertainty is an important indicator used to assess the dispersion of measured values. To describe the motion accuracy of the HSVSS, the MCM can be used to evaluate the blade displacement measurement uncertainty. The MCM is a numerical method for assessing the distribution propagation by repeatedly obtaining the probability distribution of certain input variables. Input samples can be obtained using the MCM method, based on discrete point sampling of the input variable probability distribution function (PDF). The input variable is propagated to the output variable through measurement model. Each set of discrete input samples corresponds to one output point. The estimated values of the output variables, including the interval, standard uncertainty, and other related simulation results, can be obtained from the discrete distribution of all output points.

The uncertainty and propagation of probability distribution can be evaluated using the MCM as follows:

(1) Define output Y;

(2) Determine how input variables X_1, X_2, ..., X_N are related to output Y;

(3) Establish a mathematical model of the relationship between output Y and the input variables, $Y=f(X_1, X_2, ..., X_N)$;

(4) Set PDF for X_i based on available information, including the normal distribution, uniform distribution, inverse sine distribution, and so on;

(5) Select the Monte Carlo test sample number M;

(6) Implement the MCM;

(7) Output the results;

(8) Report the results.

Before the HSVSS scanning process, the window formed by the blades must be precisely positioned. It is assumed that each of the four blades moves 6 mm in the positive direction along the X direction and 18 mm along the negative Y direction. Then, the transfer model can be used to evaluate the displacement measurement uncertainty of the blades within the range of errors and PDF of errors. The distribution of errors is shown in Tables 9 and 10.

The error terms from rigid body 1 to rigid body 2, rigid body 2 to rigid body 3, and rigid body 2′ to rigid body 3 are

Table 9 Lists of error source and PDF of Blades Y1 and Y2

Adjacent rigid body	Error source	PDF	Error vector	
			Blade Y1	Blade Y2
0-1	Assembly error of driving guide rail	Uniform	$\boldsymbol{\delta}_{\text{fab\_}y1}$ = [3 μm, 3 μm, 0, 0.017 mrad, 0, 0.017 mrad]	$\boldsymbol{\delta}_{\text{fab\_}y2}$ = [3 μm, 3 μm, 0, 0.017 mrad, 0, 0.017 mrad]
1-2	Straightness error of driving guide rail	Uniform	$\boldsymbol{\delta}_{\text{str\_}y1\_1}$ = [0.008 μm, 0, 0.007 μm, 0, 0, 0]	$\boldsymbol{\delta}_{\text{str\_}y2\_1}$ = [0.006 μm, 0, 0.007 μm, 0, 0, 0]
	Measurement feedback module error	Normal	$\boldsymbol{\delta}_{y}$ = [0, 7.501 μm, 0, 0, 0, 0]	$\boldsymbol{\delta}_{y}$ = [0, 7.501 μm, 0, 0, 0, 0]
	Error caused by air gap variation	Arcsine	$\boldsymbol{\delta}_{\text{air-gap}}$ = [0, 0, 0, 0, 0, 0.081 mrad]	$\boldsymbol{\delta}_{\text{air-gap}}$ = [0, 0, 0, 0, 0, 0.081 mrad]
2-3	Verticality error	Uniform	$\boldsymbol{\delta}_{\text{par\_}y1}$ = [0, 0, 0, 0, 0, 0.053 mrad]	$\boldsymbol{\delta}_{\text{par\_}y2}$ = [0, 0, 0, 0, 0, 0.058 mrad]
	Thermal error	Arcsine	$\boldsymbol{\delta}_{\text{therm\_}y}$ = [0.031 μm, 0.028 μm, 0.009 μm, 0, 0, 0]	$\boldsymbol{\delta}_{\text{therm\_}y}$ = [0.031 μm, 0.028 μm, 0.009 μm, 0, 0, 0]
	Inertia force deformation error	Arcsine	$\boldsymbol{\delta}_{\text{inertia force}}$ = [0, 8.3 μm, 0, 0, 0, 0]	$\boldsymbol{\delta}_{\text{inertia force}}$ = [0, 8.3 μm, 0, 0, 0, 0]
	Straightness error of driven guide rail	Uniform	$\boldsymbol{\delta}_{\text{str\_}y1\_2}$ = [0, 0.008 μm, 0.006 μm, 0, 0, 0]	$\boldsymbol{\delta}_{\text{str\_}y2\_2}$ = [0, 0.006 μm, 0.008 μm, 0, 0, 0]
0-1′	Assembly error of driving guide rail	Uniform	$\boldsymbol{\delta}_{\text{fab\_}x2}$ = [3 μm, 3 μm, 0, 0, 0.018 mrad, 0.018 mrad]	$\boldsymbol{\delta}_{\text{fab\_}x1}$ = [3 μm, 3 μm, 0, 0, 0.018 mrad, 0.018 mrad]
1′-2′	Straightness error of driving guide rail	Uniform	$\boldsymbol{\delta}_{\text{str\_}x2\_1}$ = [0, 0.003 μm, 0.007 μm, 0, 0, 0]	$\boldsymbol{\delta}_{\text{str\_}x1\_1}$ = [0, 0.004 μm, 0.006 μm, 0, 0, 0]
2′-3	Verticality error	Uniform	$\boldsymbol{\delta}_{\text{par\_}x2}$ = [0, 0, 0, 0, 0, 0.045 mrad]	$\boldsymbol{\delta}_{\text{par\_}x1}$ = [0, 0, 0, 0, 0, 0.042 mrad]
	Straightness error of driven guide rail	Uniform	$\boldsymbol{\delta}_{\text{str\_}x2\_2}$ = [0.003 μm, 0, 0.007 μm, 0, 0, 0]	$\boldsymbol{\delta}_{\text{str\_}x1\_2}$ = [0.005 μm, 0, 0.007 μm, 0, 0, 0]

Note: PDF, probability distribution function.

composed of several error sources. Therefore, the relationship between the error terms and error sources in Table 9 can be expressed as

$$\cdot \begin{bmatrix} 1 & -\delta Rz_x & \delta Ry_x & \delta x_x \\ \delta Rz_x & 1 & -\delta Rx_x & \delta y_x \\ -\delta Ry_x & \delta Rx_x & 1 & \delta z_x \\ 0 & 0 & 0 & 1 \end{bmatrix}, \tag{43}$$

$${}^{e}\boldsymbol{T}_1^2 = \begin{bmatrix} 1 & -\delta Rz_{\text{str}} & \delta Ry_{\text{str}} & \delta x_{\text{str}} \\ \delta Rz_{\text{str}} & 1 & -\delta Rx_{\text{str}} & \delta y_{\text{str}} \\ -\delta Ry_{\text{str}} & \delta Rx_{\text{str}} & 1 & \delta z_{\text{str}} \\ 0 & 0 & 0 & 1 \end{bmatrix} \qquad {}^{e}\boldsymbol{T}_2^3 = \begin{bmatrix} 1 & -\delta Rz_{\text{str}} & \delta Ry_{\text{str}} & \delta x_{\text{str}} \\ \delta Rz_{\text{str}} & 1 & -\delta Rx_{\text{str}} & \delta y_{\text{str}} \\ -\delta Ry_{\text{str}} & \delta Rx_{\text{str}} & 1 & \delta z_{\text{str}} \\ 0 & 0 & 0 & 1 \end{bmatrix}$$

Table 10 Lists of error source and PDF of Blades X1 and X2

Adjacent rigid body	Error source	PDF	Error vector	
			Blade X1	Blade X2
0-1	Assembly error of driving guide rail	Uniform	$\boldsymbol{\delta}_{\text{fab\_}x1}$ = [3 μm, 3 μm, 0, 0, 0.018 mrad, 0.018 mrad]	$\boldsymbol{\delta}_{\text{fab\_}x2}$ = [3 μm, 3 μm, 0, 0, 0.018 mrad, 0.018 mrad]
1-2	Straightness error of driving guide rail	Uniform	$\boldsymbol{\delta}_{\text{str\_}x1\_1}$ = [0, 0.004 μm, 0.006 μm, 0, 0, 0]	$\boldsymbol{\delta}_{\text{str\_}x2\_1}$ = [0, 0.003 μm, 0.007 μm, 0, 0, 0]
	Measurement feedback module error	Normal	$\boldsymbol{\delta}_{x}$ = [2.7008 μm, 0, 0, 0, 0, 0]	$\boldsymbol{\delta}_{x}$ = [2.7008 μm, 0, 0, 0, 0, 0]
2-3	Verticality error	Uniform	$\boldsymbol{\delta}_{\text{par\_}x1}$ = [0, 0, 0, 0, 0, 0.042 mrad]	$\boldsymbol{\delta}_{\text{par\_}x2}$ = [0, 0, 0, 0, 0, 0.045 mrad]
	Thermal error	Arcsine	$\boldsymbol{\delta}_{\text{therm\_}x}$ = [−0.002 μm, 0.082 μm, 0.023 μm, 0, 0, 0]	$\boldsymbol{\delta}_{\text{therm\_}x}$ = [−0.002 μm, 0.082 μm, 0.023 μm, 0, 0, 0]
	Straightness error of driven guide rail	Uniform	$\boldsymbol{\delta}_{\text{str\_}x1\_2}$ = [0.005 μm, 0, 0.007 μm, 0, 0, 0]	$\boldsymbol{\delta}_{\text{str\_}x2\_2}$ = [0.003 μm, 0, 0.007 μm, 0, 0, 0]
0-1′	Assembly error of driving guide rail	Uniform	$\boldsymbol{\delta}_{\text{fab\_}y1}$ = [3 μm, 3 μm, 0, 0.017 mrad, 0, 0.017 mrad]	$\boldsymbol{\delta}_{\text{fab\_}y2}$ = [3 μm, 3 μm, 0, 0.017 mrad, 0, 0.017 mrad]
1′-2′	Straightness error of driving guide rail	Uniform	$\boldsymbol{\delta}_{\text{str\_}y1\_1}$ = [0.008 μm, 0, 0.007 μm, 0, 0, 0]	$\boldsymbol{\delta}_{\text{str\_}y2\_1}$ = [0.006 μm, 0, 0.007 μm, 0, 0, 0]
2′-3	Verticality error	Uniform	$\boldsymbol{\delta}_{\text{par\_}y1}$ = [0, 0, 0, 0, 0, 0.053 mrad]	$\boldsymbol{\delta}_{\text{par\_}y2}$ = [0, 0, 0, 0, 0, 0.058 mrad]
	Straightness error of driven guide rail	Uniform	$\boldsymbol{\delta}_{\text{str\_}y1\_2}$ = [0, 0.008 μm, 0.006 μm, 0, 0, 0]	$\boldsymbol{\delta}_{\text{str\_}y2\_2}$ = [0, 0.006 μm, 0.008 μm, 0, 0, 0]

Note: PDF, probability distribution function.

$$\cdot\begin{bmatrix} 1 & -\delta Rz_{\text{therm}} & \delta Ry_{\text{therm}} & \delta x_{\text{therm}} \\ \delta Rz_{\text{therm}} & 1 & -\delta Rx_{\text{therm}} & \delta y_{\text{therm}} \\ -\delta Ry_{\text{therm}} & \delta Rx_{\text{therm}} & 1 & \delta z_{\text{therm}} \\ 0 & 0 & 0 & 1 \end{bmatrix}\cdot\begin{bmatrix} 1 & -\delta Rz_{\text{par}} & \delta Ry_{\text{par}} & \delta x_{\text{par}} \\ \delta Rz_{\text{par}} & 1 & -\delta Rx_{\text{par}} & \delta y_{\text{par}} \\ -\delta Ry_{\text{par}} & \delta Rx_{\text{par}} & 1 & \delta z_{\text{par}} \\ 0 & 0 & 0 & 1 \end{bmatrix}, \tag{44}$$

$${}^{e}\boldsymbol{T}_{2'}^{3} = \begin{bmatrix} 1 & -\delta Rz_{\text{str}} & \delta Ry_{\text{str}} & \delta x_{\text{str}} \\ \delta Rz_{\text{str}} & 1 & -\delta Rx_{\text{str}} & \delta y_{\text{str}} \\ -\delta Ry_{\text{str}} & \delta Rx_{\text{str}} & 1 & \delta z_{\text{str}} \\ 0 & 0 & 0 & 1 \end{bmatrix}\cdot\begin{bmatrix} 1 & -\delta Rz_{\text{par}} & \delta Ry_{\text{par}} & \delta x_{\text{par}} \\ \delta Rz_{\text{par}} & 1 & -\delta Rx_{\text{par}} & \delta y_{\text{par}} \\ -\delta Ry_{\text{par}} & \delta Rx_{\text{par}} & 1 & \delta z_{\text{par}} \\ 0 & 0 & 0 & 1 \end{bmatrix}. \tag{45}$$

The relationship between error terms and error sources in Table 9 can be expressed as

$$
{}^{e}\boldsymbol{T}_{1}^{2}=\begin{bmatrix}1 & -\delta Rz_{\mathrm{str}} & \delta Ry_{\mathrm{str}} & \delta x_{\mathrm{str}}\\ \delta Rz_{\mathrm{str}} & 1 & -\delta Rx_{\mathrm{str}} & \delta y_{\mathrm{str}}\\ -\delta Ry_{\mathrm{str}} & \delta Rx_{\mathrm{str}} & 1 & \delta z_{\mathrm{str}}\\ 0 & 0 & 0 & 1\end{bmatrix}\cdot\begin{bmatrix}1 & -\delta Rz_{y} & \delta Ry_{y} & \delta x_{y}\\ \delta Rz_{y} & 1 & -\delta Rx_{y} & \delta y_{y}\\ -\delta Ry_{y} & \delta Rx_{y} & 1 & \delta z_{y}\\ 0 & 0 & 0 & 1\end{bmatrix}
$$

$$
\cdot\begin{bmatrix}1 & -\delta Rz_{\text{air-gap}} & \delta Ry_{\text{air-gap}} & \delta x_{\text{air-gap}}\\ \delta Rz_{\text{air-gap}} & 1 & -\delta Rx_{\text{air-gap}} & \delta y_{\text{air-gap}}\\ -\delta Ry_{\text{air-gap}} & \delta Rx_{\text{air-gap}} & 1 & \delta z_{\text{air-gap}}\\ 0 & 0 & 0 & 1\end{bmatrix}, \tag{46}
$$

$$
{}^{e}\boldsymbol{T}_{2}^{3}=\begin{bmatrix}1 & -\delta Rz_{\mathrm{str}} & \delta Ry_{\mathrm{str}} & \delta x_{\mathrm{str}}\\ \delta Rz_{\mathrm{str}} & 1 & -\delta Rx_{\mathrm{str}} & \delta y_{\mathrm{str}}\\ -\delta Ry_{\mathrm{str}} & \delta Rx_{\mathrm{str}} & 1 & \delta z_{\mathrm{str}}\\ 0 & 0 & 0 & 1\end{bmatrix}\cdot\begin{bmatrix}1 & -\delta Rz_{\mathrm{therm}} & \delta Ry_{\mathrm{therm}} & \delta x_{\mathrm{therm}}\\ \delta Rz_{\mathrm{therm}} & 1 & -\delta Rx_{\mathrm{therm}} & \delta y_{\mathrm{therm}}\\ -\delta Ry_{\mathrm{therm}} & \delta Rx_{\mathrm{therm}} & 1 & \delta z_{\mathrm{therm}}\\ 0 & 0 & 0 & 1\end{bmatrix}
$$

$$
\cdot\begin{bmatrix}1 & -\delta Rz_{\mathrm{par}} & \delta Ry_{\mathrm{par}} & \delta x_{\mathrm{par}}\\ \delta Rz_{\mathrm{par}} & 1 & -\delta Rx_{\mathrm{par}} & \delta y_{\mathrm{par}}\\ -\delta Ry_{\mathrm{par}} & \delta Rx_{\mathrm{par}} & 1 & \delta z_{\mathrm{par}}\\ 0 & 0 & 0 & 1\end{bmatrix}\cdot\begin{bmatrix}1 & -\delta Rz_{\text{inertia force}} & \delta Ry_{\text{inertia force}} & \delta x_{\text{inertia force}}\\ \delta Rz_{\text{inertia force}} & 1 & -\delta Rx_{\text{inertia force}} & \delta y_{\text{inertia force}}\\ -\delta Ry_{\text{inertia force}} & \delta Rx_{\text{inertia force}} & 1 & \delta z_{\text{inertia force}}\\ 0 & 0 & 0 & 1\end{bmatrix}, \tag{47}
$$

$$
{}^{e}\boldsymbol{T}_{2'}^{3}=\begin{bmatrix}1 & -\delta Rz_{\mathrm{str}} & \delta Ry_{\mathrm{str}} & \delta x_{\mathrm{str}}\\ \delta Rz_{\mathrm{str}} & 1 & -\delta Rx_{\mathrm{str}} & \delta y_{\mathrm{str}}\\ -\delta Ry_{\mathrm{str}} & \delta Rx_{\mathrm{str}} & 1 & \delta z_{\mathrm{str}}\\ 0 & 0 & 0 & 1\end{bmatrix}\cdot\begin{bmatrix}1 & -\delta Rz_{\mathrm{par}} & \delta Ry_{\mathrm{par}} & \delta x_{\mathrm{par}}\\ \delta Rz_{\mathrm{par}} & 1 & -\delta Rx_{\mathrm{par}} & \delta y_{\mathrm{par}}\\ -\delta Ry_{\mathrm{par}} & \delta Rx_{\mathrm{par}} & 1 & \delta z_{\mathrm{par}}\\ 0 & 0 & 0 & 1\end{bmatrix}. \tag{48}
$$

For the MCM, the number of samples was set as 10^6 and a 95% confidence interval was selected. The simulated displacement error distribution area of Blades X1, X2, Y1, and Y2 are shown in Fig. 22.

In summary, the blade displacement measurements with extended uncertainty (95% confidence interval) are:

The displacement measurement result of Blade X1 along X and Y directions are (5.9835, 6.0165) mm and (−18.0013, −17.9987) mm, respectively; the displacement measurement result of Blade X2 along X and Y directions are (5.9752, 6.0248) mm and (−18.0151, −17.9849) mm, respectively; the displacement measurement result of Blade Y1 along X and Y directions are (5.9941, 6.0009) mm and (−18.0164, −17.9632) mm, respectively; the displacement measurement result of Blade Y2 along X and Y directions are (5.9975, 6.0025) mm and (−18.0200, −17.9572) mm, respectively.

6 Conclusions

The HSVSS is an important part of the optical illumination system. In this paper, an error transfer model of the HSVSS based on a double-layer two-dimensional orthogonal air-floating guide was established, and the influence of each source of error on the motion error of blade was analyzed. At the same time, the maximum range of every error source were obtained by simulation and experiment and the displacement uncertainty of the blades were evaluated by the MCM.

According to the results obtained using the proposed error transfer model, the installation error of the driving rail has the largest influence on the motion accuracy of the blades in the HSVSS. Therefore, errors should be minimized during the assembly process. Finally, based on the results of the dynamic error analysis, increasing the

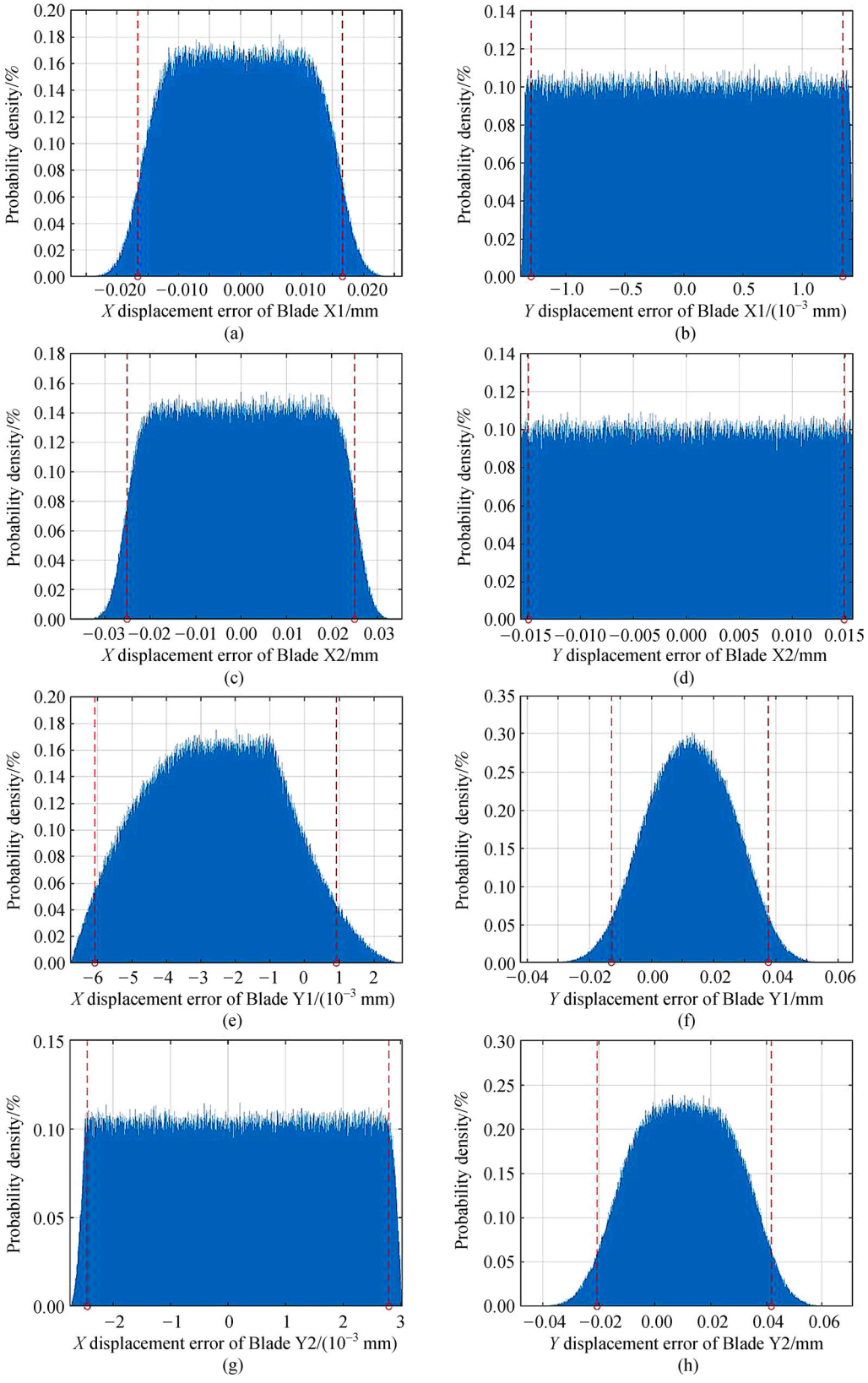

Fig. 22 Simulated displacement distributions of the blades. Displacements of (a) Blade X1 along the *X* direction, (b) Blade X1 along the *Y* direction, (c) Blade X2 along the *X* direction, (d) Blade X2 along the *Y* direction, (e) Blade Y1 along the *X* direction, (f) Blade Y1 along the *Y* direction, (g) Blade Y2 along the *X* direction, and (h) Blade Y2 along *Y* direction.

air gap stiffness of the air-floating guide rail can effectively improve the dynamic accuracy of the blade at high accelerations.

Acknowledgements This work was funded by the National Natural Science Foundation of China (Grant No. 51675136), the National Science and Technology Major Project (Grant No. 2017ZX02101006-005), the China Postdoctoral Science Foundation (Grant No. 2018T110291), and the Heilongjiang Natural Science Foundation (Grant No. E2017032).

References

1. Schmidt R H M. Ultra-precision engineering in lithographic exposure equipment for the semiconductor industry. Philosophical Transactions of the Royal Society A: Mathematical, Physical and Engineering Sciences, 2012, 370(1973): 3950–3972
2. Houser D C, Dong F, Perera C N, et al. Challenges in constructing EUV metrology tools to qualify the EUV masks for HVM implementation. Proceedings Volume 9661, 31st European Mask and Lithography Conference, 2015, 9661: 96610K1-9
3. Levinson H J. Lithography and mask challenges at the leading edge. Proceedings Volume 9635, Photomask Technology, 2015, 9635: 963502
4. Saber M G, Xing Z, Patel D, et al. A CMOS compatible ultracompact silicon photonic optical add-drop multiplexer with misaligned sidewall Bragg gratings. IEEE Photonics Journal, 2017, 9(3): 6601010
5. Layton C H. Principles and techniques for designing precision machines. Dissertation for the Doctoral Degree. Massachusetts: Massachusetts Institute of Technology, 1999, 38–82
6. Schwenke H, Knapp W, Haitjema H, et al. Geometric error measurement and compensation of machines-an update. CIRP Annals-Manufacturing Technology, 2008, 57(2): 660–675
7. Lee J H, Yang S H. Statistical optimization and assessment of a thermal error model for CNC machine tools. International Journal of Machine Tools and Manufacture, 2002, 42(1): 147–155
8. Kong L B, Cheung C F. Prediction of surface generation in ultra-precision raster milling of optical freeform surfaces using an integrated kinematics error model. Advances in Engineering Software, 2012, 45(1): 124–136
9. Ashok S D, Samuel G L. Modeling, measurement and evaluation of spindle radial errors in a miniaturized machine tool. International Journal of Advanced Manufacturing Technology, 2012, 59(5–8): 445–461
10. Bui C B, Hwang J, Lee C H, et al. Three-face step-diagonal measurement method for the estimation of volumetric positioning errors in a 3D workspace. International Journal of Machine Tools and Manufacture, 2012, 60: 40–43
11. Wang S, Ding X, Zhu D, et al. Measurement uncertainty evaluation in whiplash test model via neural network and support vector machine-based Monte Carlo method. Measurement, 2018, 119: 229–245
12. Lei W, Hsu Y. Accuracy enhancement of five-axis CNC machines through realtime error compensation. International Journal of Machine Tools and Manufacture, 2003, 43(9): 871–877
13. Bohez E, Ariyajunya B, Sinlapeecheewa C, et al. Systematic geometric rigid body error identification of 5-axis milling machines. Computer Aided Design, 2007, 39(4): 229–244
14. Kiridena V, Ferreira P. Mapping the effects of positioning errors on the volumetric accuracy of five-axis CNC machine tools. International Journal of Machine Tools and Manufacture, 1993, 33(3): 417–437
15. Tang H, Duan J, Zhao Q. A systematic approach on analyzing the relationship between straightness & angular errors and guideway surface in precise linear stage. International Journal of Machine Tools and Manufacture, 2017, 120: 12–19
16. Chen J, Lin S, Zhou X. A comprehensive error analysis method for the geometric error of multi-axis machine tool. International Journal of Machine Tools and Manufacture, 2016, 106: 56–66
17. Tian W, Gao W, Zhang D, et al. A general approach for error modeling of machine tools. International Journal of Machine Tools and Manufacture, 2014, 79: 17–23
18. Zhao D, Bi Y, Ke Y. An efficient error compensation method for coordinated CNC five-axis machine tools. International Journal of Machine Tools and Manufacture, 2017, 123: 105–115
19. Li J, Xie F, Liu X J. Geometric error modeling and sensitivity analysis of a five-axis machine tool. International Journal of Advanced Manufacturing Technology, 2016, 82(9–12): 2037–2051
20. Chen G, Liang Y, Sun Y, et al. Volumetric error modeling and sensitivity analysis for designing a five-axis ultra-precision machine tool. International Journal of Advanced Manufacturing Technology, 2013, 68(9–12): 2525–2534
21. Liu Y, Wan M, Xiao Q B, et al. Identification and compensation of geometric errors of rotary axes in five-axis machine tools through constructing equivalent rotary axis (ERA). International Journal of Mechanical Sciences, 2019, 152: 211–227
22. Andolfatto L, Mayer J R R, Lavernhe S. Adaptive Monte Carlo applied to uncertainty estimation in five axis machine tool link errors identification with thermal disturbance. International Journal of Machine Tools and Manufacture, 2011, 51(7–8): 618–627
23. Liu Y, Yuan M, Cao J, et al. Evaluation of measurement uncertainty in H-drive stage during high acceleration based on Monte Carlo method. International Journal of Machine Tools and Manufacture, 2015, 93: 1–9